Bioactive Materials 35 (2024) 495–516

Contents lists available at ScienceDirect

Bioactive Materials

journal homepage: www.keaipublishing.com/en/journals/bioactive-materials

# Selenomethionine in gelatin methacryloyl hydrogels: Modulating ferroptosis to attenuate skin aging

Jiachen Sun [1], Xiaoye Xie [1], Yaoyao Song [1], Tianjun Sun, Xinzhu Liu, Huageng Yuan, Chuanan Shen [*]

*Department of Burns and Plastic Surgery, Fourth Medical Center of Chinese PLA General Hospital, Beijing, 100048, China*

ARTICLE INFO

*Keywords:*
Chronic wounds
Photoaging
Hydrogels
Ferroptosis

ABSTRACT

During skin aging, the degeneration of epidermal stem cells (EpiSCs) leads to diminished wound healing capabilities and epidermal disintegration. This study tackles this issue through a comprehensive analysis combining transcriptomics and untargeted metabolomics, revealing age-dependent alterations in the *Gpx* gene family and arachidonic acid (AA) metabolic networks, resulting in enhanced ferroptosis. Selenomethionine (Se-Met) could enhance GPX4 expression, thereby assisting EpiSCs in countering AA-induced mitochondrial damage and ferroptosis. Additionally, Se-Met demonstrates antioxidative characteristics and extensive ultraviolet absorption. For the sustained and controllable release of Se-Met, it was covalently grafted to UV-responsive GelMA hydrogels via AC-PEG-NHS tethers. The Se-Met@GelMA hydrogel effectively accelerated wound healing in a chronological aging mice model, by inhibiting lipid peroxidation and ferroptosis with augmented GPX4 expression. Moreover, in a photoaging model, this hydrogel significantly mitigated inflammatory responses, extracellular matrix remodeling, and ferroptosis in UV-exposed mice. These characteristics render Se-Met@GelMA hydrogel valuable in practical clinical applications.

## 1. Introduction

Aging is a burgeoning issue worldwide, from developed to developing countries. The WHO reports that by 2050, the population aged over 60 will reach approximately 2 billion, constituting 22% of the global population. The skin, being the largest and outermost organ, plays vital roles in protection, excretion, and sensory perception. Skin aging results from a complex interplay of intrinsic aging and photoaging processes. This aging is marked by the deterioration of epidermal stem cells (EpiSCs), leading to diminished wound healing capabilities and loss of normal epidermal structure. Such impairment in wound healing contributes to disrupted wound healing process and the formation of chronic hard-to-heal wounds, posing significant healthcare challenges and economic burdens globally. The deterioration of normal epidermal structure, evidenced by the appearance of wrinkles, hyperpigmentation, and desquamation, may accelerate the degeneration of EpiSCs through the disruption of their natural niche [1].

Here, we performed an integrative transcriptomics and metabolomics study on EpiSCs of different ages. The omics analysis highlights the age-dependent metabolic adaptations of arachidonic acid (AA) and elevated levels of ferroptosis, manifested by increased lipid peroxidation and decreased Glutathione Peroxidase 4 (GPX4) expression. Extra AA feeding was confirmed to induce ferroptosis with mitochondrial destruction in EpiSCs lacking GPX4 both in vitro and in middle-aged mice. Characterized by antioxidative and Ultraviolet Radiation (UV)-absorbing properties, Selenomethionine (Se-Met) showed its protective effect on EpiSCs by reverting GPX4 expression. Further, Se-Met was covalently immobilized within the UV-responsive Gelatin methacryloyl (GelMA) hydrogels via acrylate-functionalized polyethylene glycol (AC-PEG) tethers, with good plasticity, release properties, and mechanical properties. Se-Met@GelMA hydrogel has been shown to effectively accelerate wound healing in chronological aging mice model, by inhibiting lipid peroxidation and ferroptosis. Furthermore, in the photoaging model, this hydrogel also demonstrates significant efficacy in

Peer review under responsibility of KeAi Communications Co., Ltd.

* Corresponding author.
*E-mail addresses:* Sunshinejiachen@outlook.com (J. Sun), xxy.n1@163.com (X. Xie), yaoyao_430@126.com (Y. Song), 13811669318@139.com (T. Sun), 14743791177@163.com (X. Liu), yuanhuageng2022@163.com (H. Yuan), shenchuanan@301hospital.com.cn (C. Shen).
[1] These authors contributed equally to the manuscript.

https://doi.org/10.1016/j.bioactmat.2024.02.013
Received 26 December 2023; Received in revised form 8 February 2024; Accepted 9 February 2024

mitigating inflammation, extracellular matrix remodeling, and ferroptosis in UV-exposed mice.

## 2. Results

### 2.1. Age-dependent transcriptomic adaptations in EpiSCs

During aging, the major molecular adaptations are the damaged genetic stability due to reduced DNA repair capacity, impaired proliferative potential due to loss of stemness, and cellular plasticity-related alternations in DNA-methylation patterns, etc. [2,3] Besides, the metabolic adaptations also play an important part in aging, manifested as the progressively impaired function and morphology of mitochondria during aging, accompanied by the altered metabolic profiles [4–6]. Mainly located in the basal layer of the epidermis, EpiSCs were of particular importance in maintaining the integrity of the skin and facilitating re-epithelialization during wound healing [7]. Therefore, we conducted transcriptomic and metabolomic analyses on EpiSCs from mice of various ages to identify precise targets for intervening in the aging process (Fig. 1A).

With nine samples per group, EpiSCs from the dorsal skin of young and aged male mice were harvested, enzymatically digested, and subsequently sorted via flow cytometry for mRNA sequencing. The principal component analysis (PCA) segregated the EpiSCs populations into distinct clusters representing young and old age groups (Fig. 1B). The first principal component (PC1) accounted for 37.8% and the second (PC2) for 14.2% of the variance, indicative of substantial biological variations possibly compounded by technical differences between the samples. Using DESeq2 for the analysis of differential expressed genes (DEGs) with a threshold of q-value $<0.05$ and Fold Change (FC) $\geq 2$ or FC $\leq 0.5$, we identified 1657 genes upregulated and 643 genes downregulated in the aged EpiSCs (Fig. S1A). Kyoto Encyclopedia of Genes and Genomes (KEGG) pathway enrichment identified a significant overrepresentation of genes across metabolism, environmental information processing, organismal systems, and cellular processes categories, as visualized in the bubble plot of the top 25 pathways with the smallest $p$ values (Fig. S1B). This highlights the pivotal role of metabolic alterations in the aging process of EpiSCs. Further detailed examination of the metabolic class via KEGG analysis (Fig. 1C) revealed the most pronounced changes within the arachidonic acid metabolism pathway, which exhibited the highest gene count ($n = 17$, $p = 0.005$). This was closely followed by glycerophospholipid metabolism ($n = 16$, $p = 0.028$) and ether lipid metabolism ($n = 13$, $p < 0.001$), all indicating a significant shift in lipid-related pathways during the aging process of EpiSCs. Gene Ontology (GO) analysis highlighted the top 15 molecular functions ($q < 0.05$), revealing a notable enrichment in ion transmembrane transporter activity and ion channel activity (Fig. 1D). Furthermore, pathways related to the metabolism and transport of lipids and lipophilic molecules were significantly enriched, indicating their substantial involvement in the aging process of EpiSCs. These findings imply a potential compromise in the normal cellular membrane structure and transmembrane transport function of aging EpiSCs, underlining the importance of cellular membrane integrity and lipid homeostasis in the maintenance of EpiSC functionality during aging.

Upon further investigation into the metabolic pathways, the age-related gene expression patterns were displayed in Gene Set Enrichment Analysis (GSEA), utilizing |normalized ES (nES)| $> 1$, and $q$ value $< 0.30$ as the screening criteria. Fig. 1E revealed the top ten metabolic pathways, highlighting alterations in lipid metabolism during the aging process of EpiSCs. Notably, the arachidonic acid metabolism pathway ($|nES| = 1.264$, $q = 0.146$), the Phospholipase D (PLD) signaling pathway ($|nES| = 1.607$, $q = 0.023$) and the cytochrome P450 pathways ($|nES| = 1.394$, $q = 0.073$) exhibit substantial changes, all of which are tightly linked to the metabolism of AA. Alterations in PLD activity are closely correlated with changes in the AA content, via its critical role in the conversion of phosphatidylcholine (PC) to phosphatidic acid (PA), a precursor molecule in the biosynthesis of AA. The cytochrome P450 pathway, a pivotal component in the metabolic processing of pharmaceuticals, toxins, and endogenous substances, catalyzes the oxidation of AA. This step is fundamental in transforming AA into a spectrum of secondary metabolites, including biologically active compounds such as prostaglandins (PGs) and leukotrienes (LTs), which are essential in various physiological and inflammatory responses.

As an omega-6 polyunsaturated fatty acid, AA mainly exists in the form of phospholipids on cell membranes and plays a complex role in skin structure maintenance and wound healing via inflammation, lipid peroxidation, apoptosis, autophagy, or ferroptosis [8–11]. Free AA is mainly generated by the hydrolysis of membrane phospholipids by phospholipase A2 (PLA2), or the membrane phospholipids are first degraded by phospholipase C (PLC) to diacylglycerol, which is then further decomposed by diacylglycerol lipase to generate free AA. Considering the pivotal role of AA metabolic adaptations in the aging of EpiSCs, we further validated the expression level changes of associated genes enriched by KEGG and GO analyses through RT-qPCR (Fig. 1F). The aged EpiSCs displayed an upregulation of genes within the *Pla2* family, whereas genes in the *Gpx* and *Gst* families exhibited a notable downregulation.

The upregulation of *Pla2g4d*, *Pla2g4e*, and *Pla2g4f* expression suggests an increase in PLA2 activity. This may accelerate the hydrolysis of ester bonds in phosphatidylcholine, leading to increased release of AA and its conversion into the downstream metabolites, such as PGs, LTs, and thromboxanes (TXs) [12]. Further, *Pla2g4d* and *Pla2g4e* play important roles in immune responses and inflammation, while *Pla2g4f* is involved in cell apoptosis and cancer development [13–15]. On the contrary, *Gpx3*, *Gpx4*, *Gpx7*, and *Gpx8* are members of the GPX family that possess antioxidant activity by transferring hydrogen peroxide into $H_2O$ and thus reducing the production of ROS or lipid peroxidation [16]. Their downregulation may indicate a decrease in antioxidant capacity of the GPX family in aged EpiSCs.

The activity of glutathione transferase (GST) has been shown to decrease in aging cells, leading to a decrease in GSH content [17]. Encoding the subfamily 1 Theta class of GST, GSTT1 and GSTT2 could regulate mitochondrial and oxidative stress responses through the p38-MK2 pathway, and have been identified as makers of aging, as evidenced by the deceased expression of *Gstt1* and *Gstt2* in the livers of aging rats [18]. Our RT-qPCR results confirmed that *Gstt1* and *Gstt2* were transcriptionally reduced in aged EpiSCs, which may partially explain the decrease in GSH content in aging skin.

### 2.2. Age-dependent metabolic adaptations in EpiSCs

Inspired by the transcriptomic data, we further conducted the untargeted metabolomic analysis of the mice EpiSCs of different ages. Polar metabolite extracts were analyzed by flow injection time-of-flight mass spectrometry as described before [19]. A total of 1127 metabolites were identified, with a close association with the metabolism of amino acids, lipids, and carbohydrates reflected by the KEGG analysis (Fig. S2A). 440 metabolites could be putatively annotated in human metabolome database (HMDB), based on the accurate-mass, isotopologue abundance and cross-correlation (Fig. 2A), including 149 lipids and lipid-like molecules (33.86%), 109 organic acids and derivatives (24.09%), 51 organoheterocyclic compounds (11.59%), etc. The LIPID MAPS database provided annotation to 218 lipids and lipid-like metabolites (Fig. 2B), revealing a significant enrichment of fatty acyls (73, 33.49%) and Glycerophospholipids (100, 45.87%). These data highlight the substantial prevalence of these lipid classes in the metabolite spectrum of EpiSCs aging.

Using the supervised discriminant analysis method (OPLS-DA), our results revealed significant differences in metabolic characteristics between young and elderly EpiSCs (Fig. 2C). The model showed high stability and reliability, as indicated by the $R^2Y$ and $Q^2$ values. Based on the screening criteria of VIP $>1$, $p < 0.05$ accompanied by FC $\geq 1.5$ or

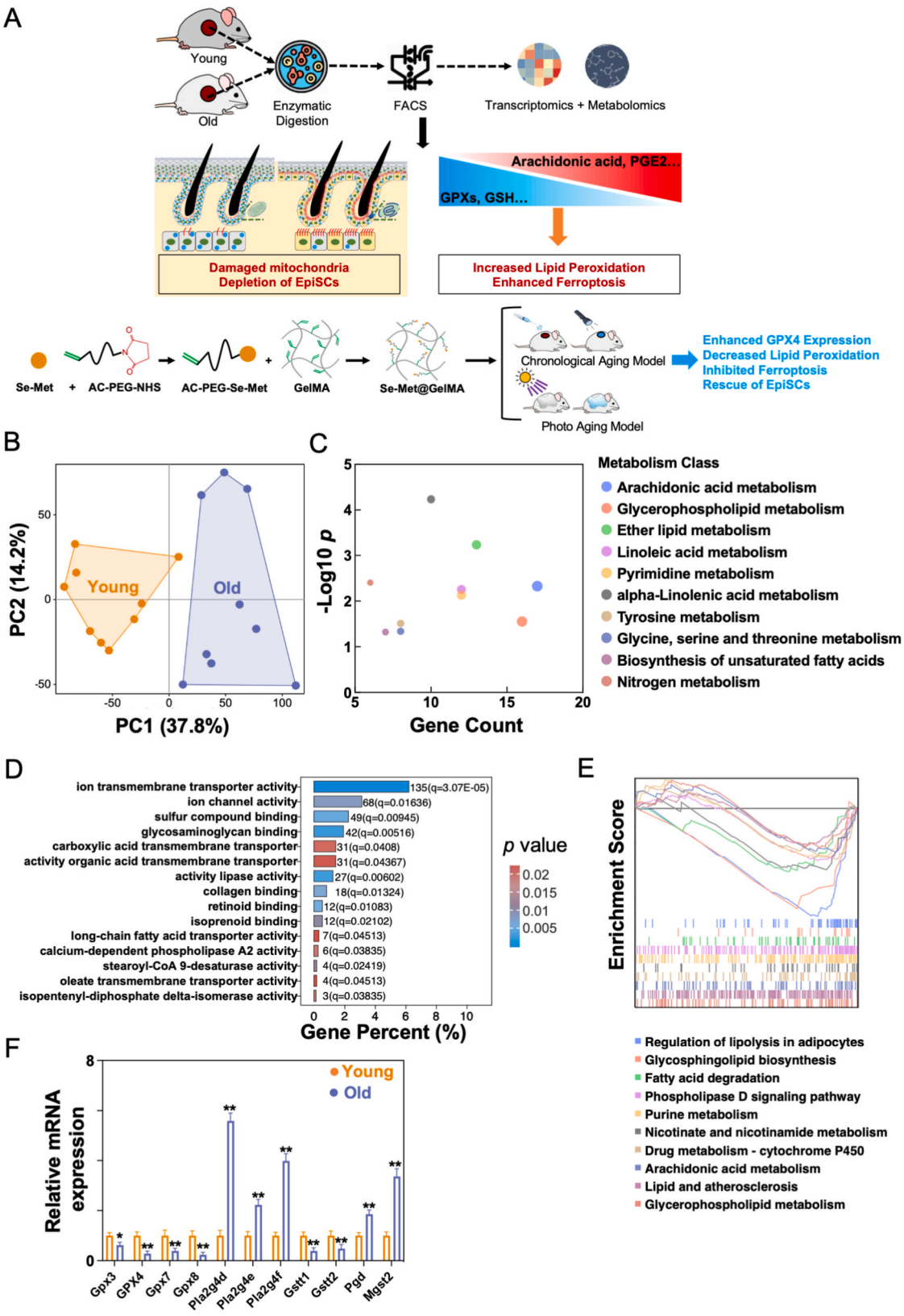


**Fig. 1.** Age-dependent gene expression adaptations in EpiSCs (A) Schematic diagram of the experiment. GPX4 was represented by blue circles, AA by red lines, and Se-Met by brown-yellow circles. (B) PCA was applied to differentiate between young and aged EpiSCs. N = 9. (C) A focused KEGG analysis on the top 10 metabolic classes. (D) GO analysis of DEGs. The top 15 age-related changes in categories of molecular function were shown. The X-axis represented the percent of enriched genes for each item. (E) GSEA identified the most significantly altered metabolic pathways in the aging process of EpiSCs. (F) RT-qPCR validation of key genes in the AA metabolism pathways in the EpiSCs of young and aged mice. N = 6. $^{*}p < 0.05$, $^{**}p < 0.01$, versus the young group.

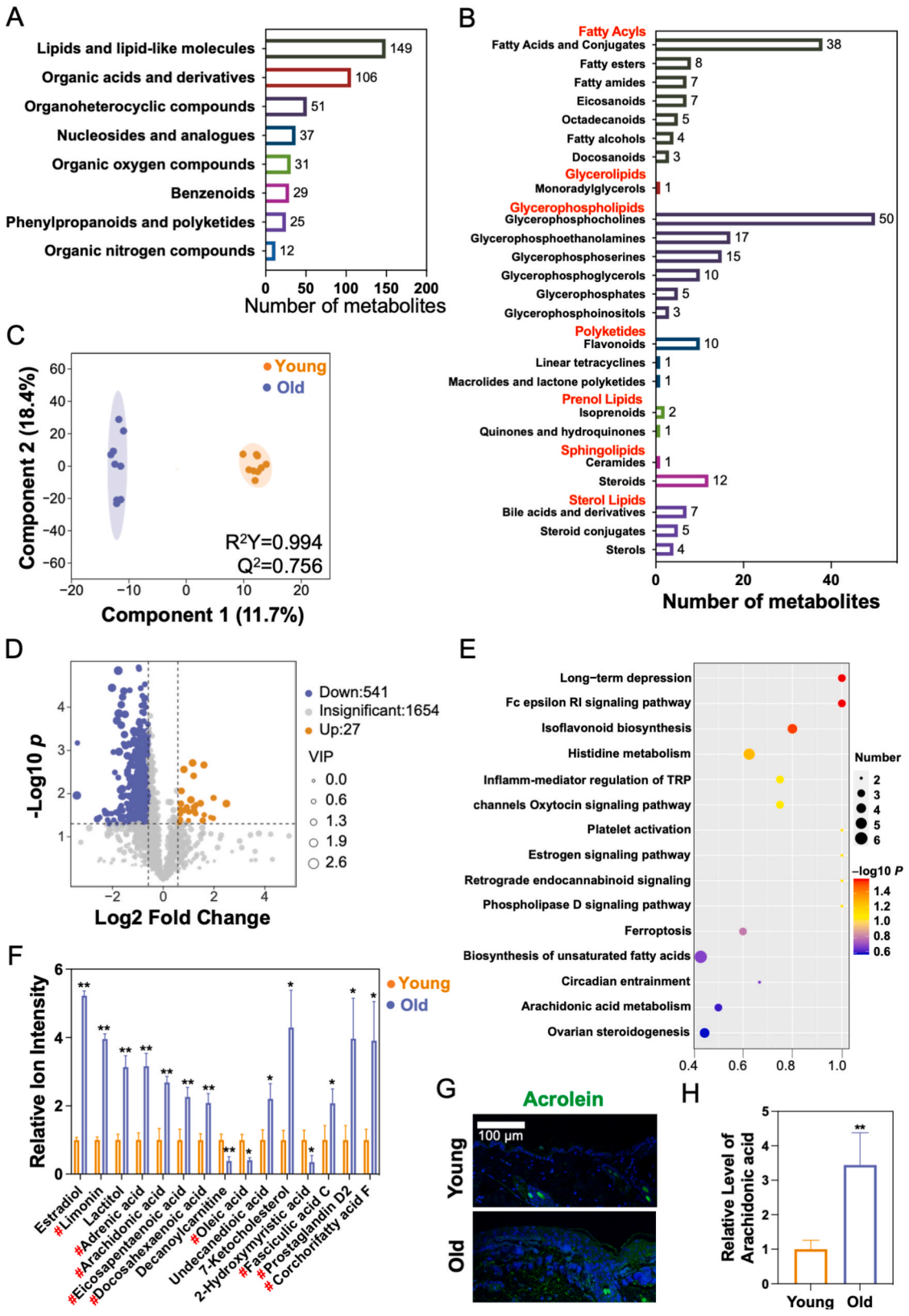


**Fig. 2.** Age-dependent metabolic adaptations in EpiSCs (A), (B) All detected metabolites were annotated in HMDB (A) and LIPID MAPS database (B). (C) Supervised discriminant analysis (OPLS-DA) was used to reduce the dimensionality of the metabolic data of each sample, and distinguish between the samples. $R^2Y$ and $Q^2$ were used to evaluate the goodness of fit and predictability of the model, respectively. N = 9. (D) Volcano plot of the DEMs. (E) KEGG analysis of the DEMs, showing the potentially related pathways and cell functions. (F) Lipids and lipid-like molecules within the DEMs, with red # indicating unsaturated lipids. $^*p < 0.05$, $^{**}p < 0.01$, versus the young group. (G) Immunofluorescence staining of young and aged mice skin with antibodies against acrolein to label peroxidation products of unsaturated lipids. Sections were co-stained with DAPI (blue) to visualize nuclei. N = 6. Scale bar, 100 μm. (H) ELISA was performed to detect AA content in the EpiSCs of young and aged mice. N = 6. $^{**}p < 0.01$, versus the young group.

FC ≤ 0.67, there was totally 568 differential DEMs, including 27 upregulated and 541 downregulated DEMs (Fig. 2D). KEGG analysis was utilized to identify all DEMs-relevant signaling pathways and cellular functions, with the top 15 pathways shown in Fig. 2E. Several metabolic pathways were enriched, including isoflavonoid biosynthesis, histidine metabolism, inflamm-mediator regulation of Transient Receptor Potential (TRP), biosynthesis of unsaturated fatty acid, AA metabolism, and ovarian steroidogenesis, etc.

In view of the important role of lipids in sustaining the integrity of the epidermal barrier, our study delved deeper into the age-associated alterations in lipids present within DEMs (Fig. 2F). Notably, we observed an enrichment of unsaturated metabolites (marked with red #), accounting for 9/17 of the differentially expressed lipids and lipid-like molecules. The expression of all the unsaturated prenol lipids and fatty acyls increased in aged EpiSCs, and only oleic acid, which was associated with longer lifespan, decreased [20]. As for the class of steroids and the derivatives, the expression of 7-ketocholesterol was increased in aged EpiSCs (FC = 4.29, $p < 0.05$, VIP = 1.29). As a toxic oxysterol associated with many metabolic diseases, 7-ketocholesterol is the most commonly seen reaction product of cholesterol and oxygen radicals, and is the most concentrated oxysterol found in the blood and arterial plaques of coronary artery disease patients [21]. Also, the formation of 7-ketocholesterol could be considered as the consequence of mitochondrial and peroxisomal dysfunction, leading to increased oxidative stress, which is accentuated with age [22].

As a lipid peroxidation product of polyunsaturated fatty acids, the level of acrolein in the skin can be used to reflect the content of polyunsaturated fatty acids [23,24]. And the immunofluorescence experiment confirmed an increase in acrolein in the epidermis of the aged mice ($p < 0.01$, Fig. 2G, Fig. S2B). The Enzyme-Linked Immunosorbent Assay (ELISA) assay demonstrated an elevated expression of AA and the downstream PGE2 in the EpiSCs of elderly mice compared to their younger counterparts ($p < 0.01$, Fig. 2H, Fig. S2C).

### 2.3. Age-related adaptations in cell death modes of EpiSCs

Through comprehensive analysis of transcriptomics and metabolomics, it was found that the aging EpiSCs exhibited decreased *Gpx* family expression, coupled with an increased content of unsaturated lipids, notably AA. The integrated effects of these age-dependent transcriptional and metabolic adaptations on EpiSCs and epidermis remain unknown.

Skin specimens from both mice and humans were obtained for analysis of age-related changes in epidermal morphology and cell death modes. In aged mice, a reduction in hair coverage was observed macroscopically (Fig. 3A), along with a significant decrease in epidermal thickness microscopically from (55.22 ± 8.43) μm in the young to only (21.57 ± 4.73) μm in the aged (Fig. 3B, Fig. S3A, $p < 0.01$). Meanwhile, the epidermis of young mice had more cell layers with a clear structure of each layer, and the boundary between the epidermis and dermis was obvious; the epidermis of aged mice had fewer cell layers, with blurred boundary between the epidermis and dermis (Fig. 3B). Additionally, a visible decrease in the number of EpiSCs in the basal layer of the epidermis was unneglectable.

λH2AX and c-Myc were employed to reflect age-related changes in DNA damage levels and repair capacity, and were found to be increased in the aging epidermis of both mice and humans (Fig. 3C–F, $p < 0.05$), indicating increased DNA damage and impaired repair capacity. LC3B was used to reflect cellular autophagy levels, and LC3B-positive cells were barely seen in the epidermis of both young and aged mice ($p > 0.05$); human epidermis exhibited a certain amount of LC3B-positive EpiSCs, but there was no statistically significant change with age ($p > 0.05$). NLRP3 was used to reflect changes in cellular pyroptosis, but no significant changes were observed in the epidermis of mice and humans of different ages ($p > 0.05$). As for apoptosis (Fig. 3G), aged mice exhibited an increased proportion of TUNEL-positive EpiSCs ($p < 0.01$), but this age-related change was not observed in human epidermis ($p > 0.05$). Given the general decreased gene expression of *Gpx* family revealed by the transcriptomic sequencing, GPX4 was selected to reflect the potential changes in cellular ferroptosis. GPX4 was predominantly expressed in the epidermis, and its expression exhibited an age-dependent decrease in both mice and human ($p < 0.01$). Western Blot experiments further confirmed the reduced expression of GPX4 in the epidermis of aged mice (Fig. 3H, Fig. S3B, $p < 0.01$). Correspondingly, the aging epidermis of mice also showed a decrease in GPX4 enzyme activity (Fig. S3C, $p < 0.01$).

### 2.4. Enhanced lipid peroxidation and ferroptosis in aged epidermis

Human and mice epidermis exhibited different age-dependent patterns of apoptosis, but both of mice and human showed a decreased GPX4 expression, suggesting further focus on ferroptosis during the aging process of the epidermis. As an α, β-unsaturated hydroxyalkenal, 4-Hydroxynonenal (4-HNE) is generally used as a marker of lipid peroxidation during ferroptosis [25]. We found that 4-HNE presented in the epidermis of young mice but mainly not the basal layer; the aged epidermis had a whole-layer expression of 4-HNE, indicating that the EpiSCs were involved in ferroptosis (Fig. 4A and B, $p < 0.01$). Further examination in mice samples confirmed the increased ferroptosis in aged epidermis, as evidenced by decreased levels of GSH (Fig. 4C, $p < 0.01$) and superoxide dismutase (SOD) activity (Fig. S4, $p < 0.01$), as well as increased levels of malondialdehyde (MDA) adducts (Fig. 4D, $p < 0.01$).

Skin samples from individuals of different ages were obtained for further verification of the lipid peroxidation, with CK14 employed to label EpiSCs with red fluorescence (Fig. 4E). The fluorescence intensity of 4-HNE was divided by the intensity of CK14 to reflect the age-related changes in the lipid peroxidation of EpiSCs (Fig. 4F). In the basal layer of the epidermis of 29-, 31-, and 32-year-old males (29 M, 31 M, and 32 M), there was a continuous distribution of CK14-positive EpiSCs with little expression of 4-HNE. As for the basal layer of the epidermis of a 50-year-old female (50 Fe), CK14-positive cells exhibited increased expression of 4-HNE, shown as yellow fluorescence resulting from the overlap of red ($CK14^+$) and green ($4\text{-}HNE^+$) fluorescence. In the basal layer of a 64-year-old male (64 M), EpiSCs showed decreased expression of CK14, and 4-HNE was not only expressed in CK14-positive cells but also widely distributed in the CK14-absent region, suggesting that areas with high expression of 4-HNE may lead to the depletion of $CK14^+$ EpiSCs. The scatter plot further demonstrates the co-localization relationship between $CK14^+$ and $4\text{-}HNE^+$ expression in the epidermis of different ages (Fig. 4E). Kendall's Tau-b rank correlation value (τ-b) was used as an evaluation index, with values closer to 1 indicating better co-localization characteristics [26]. The increasing τ-b with age represented the elevated level of lipid peroxidation in EpiSCs during aging.

Transmission electron microscopy (TEM) was applied to detect the ultrastructural changes in EpiSCs in different age groups (Fig. 4G). In the epidermis of the aged mice, the polarity of EpiSCs was lost and individual EpiSCs exhibited a greater degree of variability. Additionally, cell junctions between neighboring EpiSCs were disrupted, resulting in an increased intercellular space (indicated by red arrows). Furthermore, the volume of mitochondria in aged EpiSCs was reduced with increased membrane density, while the number of mitochondrial cristae was significantly decreased compared to the young counterparts (indicated by green arrows). All these ultrastructural changes in aged EpiSCs were consistent with cellar characteristics of ferroptosis.

### 2.5. Arachidonic acid evoked the ferroptosis of GPX4-deficient EpiSCs

With the ferroptosis of aging EpiSCs confirmed, we integrated transcriptomic and metabolic data and further investigate the effects of decreased GPX4 and increased AA on the ferroptosis of aging EpiSCs (Fig. 5A). We first generated $Gpx4^{-/-}$ EpiSCs by CRISPR Cas9 editing of exon 1, which resulted in almost no cell survival of EpiSCs and thus

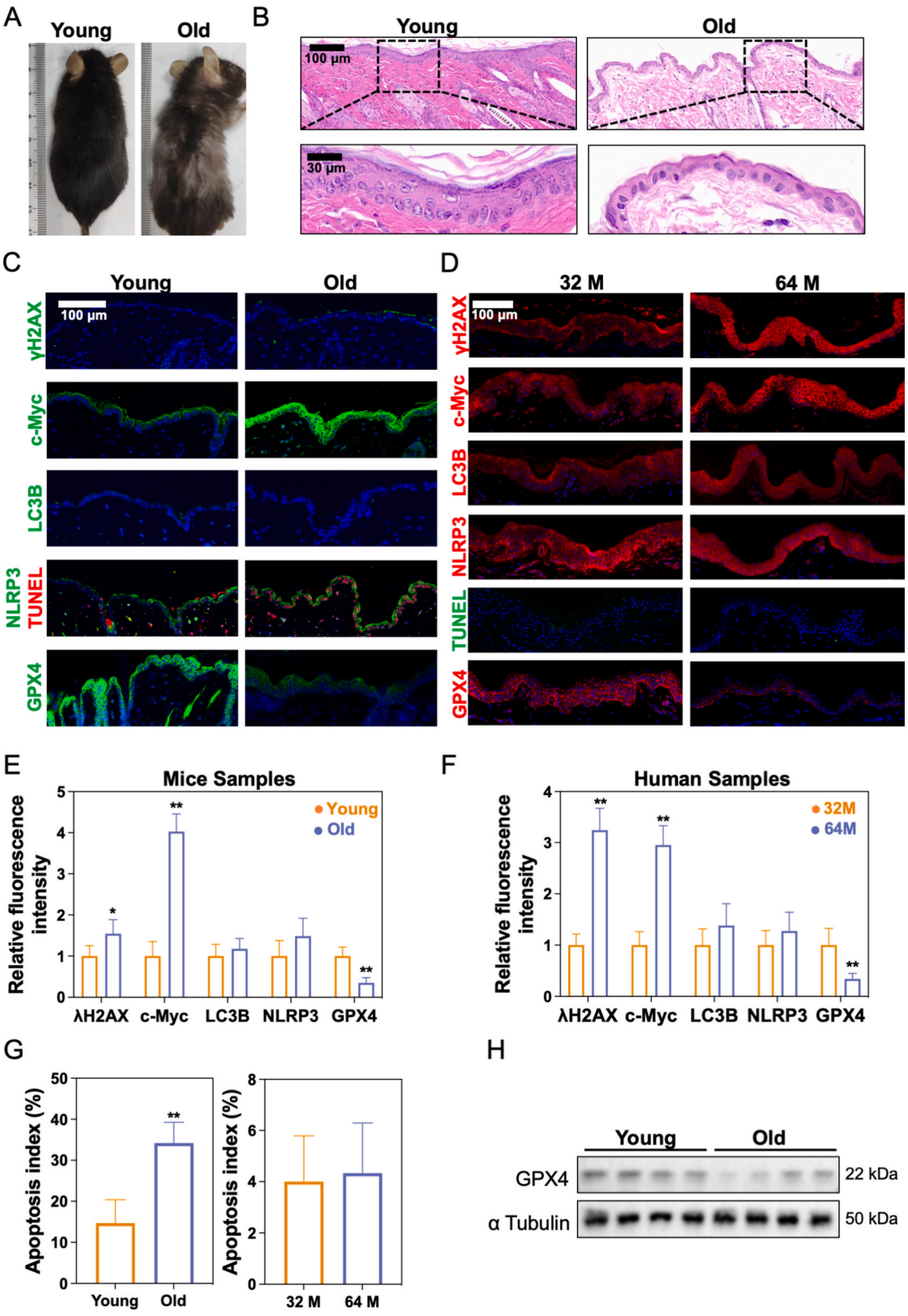


**Fig. 3.** Age-related adaptations in cell death modes in the epidermis (A) Representative photograph of young and old mice. (B) HE staining of mice skin of different ages. The box area adjacent to each photographs shows an enlarged version of the black square. N = 6. Scale bar, 100 μm and 30 μm. (C)–(G) Immunofluorescence analysis of different cell death modes in mouse and human skin samples. γH2AX and c-Myc were used as the markers of DNA damage and repair ability. LC3B, NLRP3, TUNEL, and GPX4 were respectively key proteins in autophagy, pyroptosis, apoptosis, and ferroptosis. Scale bar, 100 μm. For mouse samples, N = 6. For human samples, N = 5. *$p < 0.05$, **$p < 0.01$, versus the young or 32 M group. 32 M, 32-year-old male; 64 M, 64-year-old male. (H) Western Blot analysis of GPX4 protein levels in the epidermis of young and old mice. N = 6.

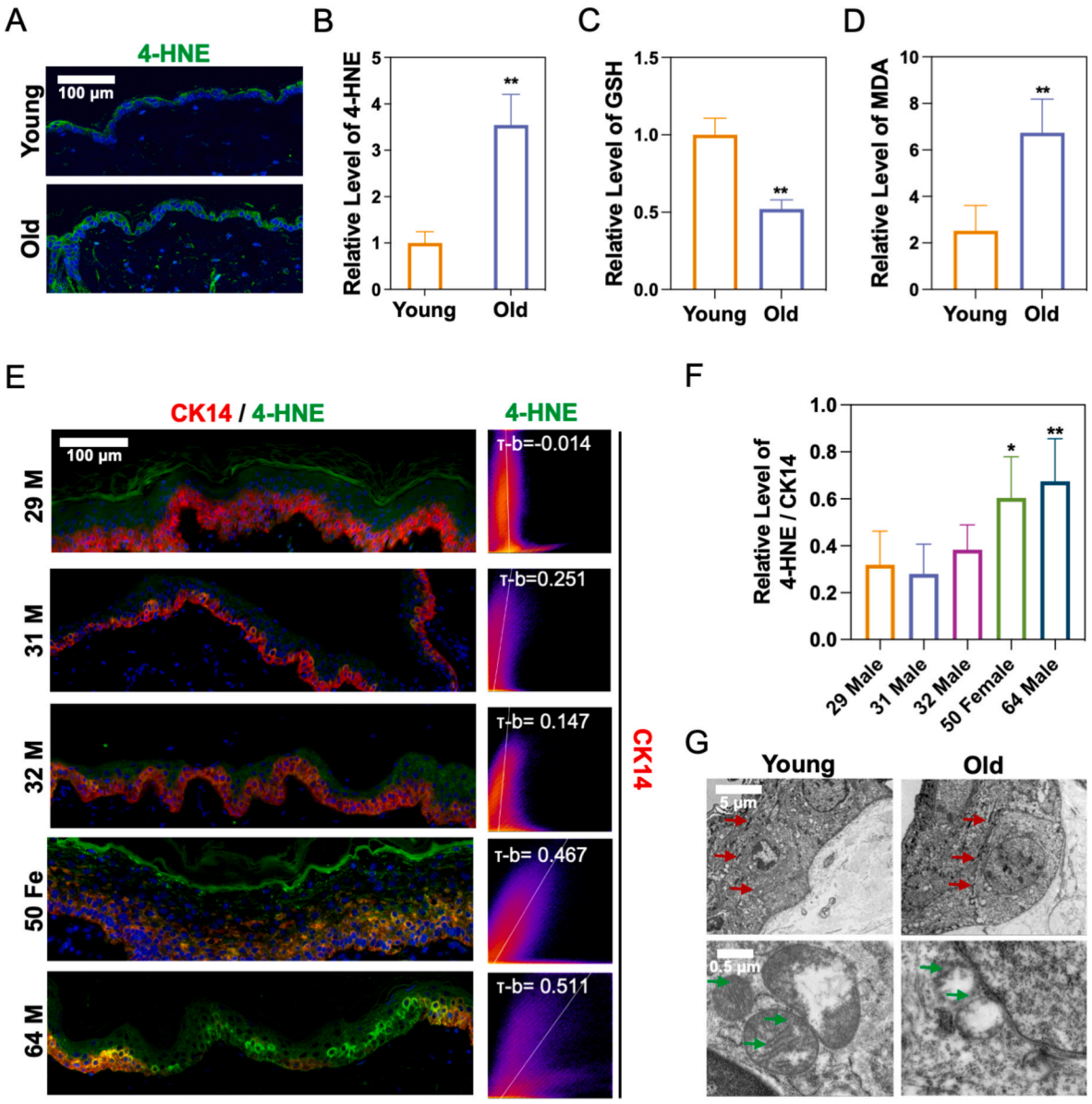


**Fig. 4.** Enhanced lipid peroxidation and ferroptosis in aged epidermis (A), (B) Immunofluorescence staining was used to label lipid peroxidation products in young and aged mice skin with antibodies against 4-HNE, and co-stained with DAPI to visualize nuclei. N = 6. Scale bar, 100 μm $^{**}p < 0.01$ versus the young group. (C), (D) The epidermis of young and aged mice was used to measure GSH levels (C) and MDA levels (D). N = 6. $^{**}p < 0.01$ versus the young group. (E), (F) Immunofluorescence staining was performed to detect the expression of 4-HNE and the distribution of EpiSCs labeled by CK14. N = 5. Scale bar, 100 μm $^{*}p < 0.05$, $^{**}p < 0.01$ versus 29 M group. 29 M, 29-year-old male; 31 M, 31-year-old male; 32 M, 32-year-old male; 50 Fe, 50-year-old female; 64 M, 64-year-old male. (G) Transmission electron microscopy was performed to reflect the ultrastructural changes in EpiSCs of mice of different ages. The upper panel focuses on the changes in cell-cell junctions with age, as indicated by red arrows. The lower panel focuses on the changes in mitochondrial cristae with age, as indicated by green arrows. N = 6. Scale bar, 5 μm or 0.5 μm.

prevented further studies. Therefore, we used small-interfering RNA (*siGPX4*) to reduce but not completely abrogate GPX4 expression. And *siGPX4* silencing impaired GPX4 expression by ~65% (Fig. 5B and C, $p < 0.05$). Additional exposure to AA did not impact the enzymatic activity of GPX4 in either *siGpx4* or siCtrl EpiSCs (Fig. 5D). However, induction of additional cell death was observed in *siGPX4* EpiSCs rather than siCtrl EpiSCs (Fig. 5E). As oxidation of unsaturated fatty acids could be restricted by GPX4, we tested the impact of reduced GPX4 activity and AA exposure on EpiSCs' lipid peroxidation. Indeed, additional AA incubation deteriorated extra lipid peroxidation in *Gpx4*-deficient EpiSCs, indicated by the higher average fluorescence intensity of the BODIPY 581/591 staining (Fig. 5F) and higher levels of MDA (Fig. 5G). Additionally, *siGPX4* EpiSCs also exhibited lower levels of GSH following AA exposure compared to siCtrl EpiSCs (Fig. 5H). Considering the damage induced by AA to mitochondria, which is closely related to the function maintenance and ferroptosis of EpiSCs, we further examined changes in mitochondrial membrane potential and mitochondrial ROS levels. Deficient GPX4 expression in EpiSCs induced a decrease in mitochondrial membrane potential and an increase in mitochondrial ROS, and extra AA incubation on this basis induced further mitochondrial damage to *siGPX4* EpiSCs (Fig. 5I and J).

### 2.6. Arachidonic acid feeding triggered ferroptosis in EpiSCs of middle-aged mice

Given the fact that in daily life AA is mainly taken orally, we further investigated the effects of excessive AA intake in the diet on skin aging and EpiSCs in vivo. Considering the long period required for creating

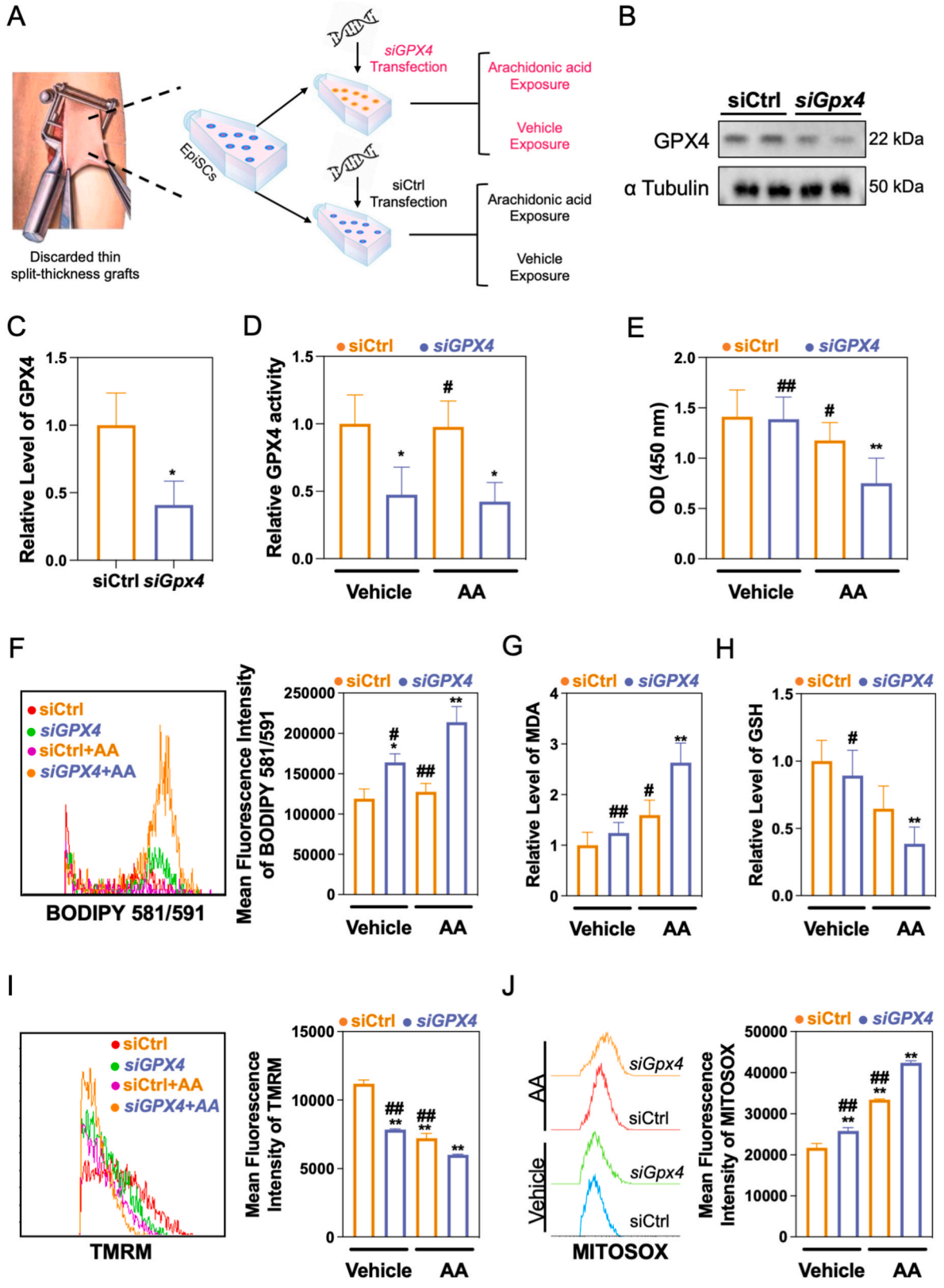


**Fig. 5.** The enhanced ferroptosis in aged epidermis was evoked by arachidonic acid (A) In vitro experiments were conducted on primary human EpiSCs with siRNA-mediated knockdown of GPX4, followed by stimulation with additional AA to investigate the level of ferroptosis. (B), (C) The effect of siRNA-mediated knockdown of GPX4 on primary human EpiSCs was evaluated by Western Blot analysis. N = 3. $^{*}p < 0.05$ versus siCtrl group. (D)–(J) Following knockdown of GPX4 in human primary EpiSCs, the cells were assessed for changes in total GPX4 enzyme activity (D), cell survival (E), lipid peroxidation levels labeled by BODIPY 581/591 (F), MDA content (G), GSH content (H), mitochondrial membrane potential reflected by TMRM (I), and mitochondrial ROS revealed by MITOSOX (J). N = 3. $^{*}p < 0.05$, $^{**}p < 0.01$ versus siCtrl group with vehicle exposure. $^{\#}p < 0.05$, $^{\#\#}p < 0.01$ versus *siGPX4* group with AA exposure.

gene-edited animals, middle-aged mice were employed whose GPX4 expression was also deteriorated compared to their young counterparts (Fig. 6A). After being orally challenged with AA for one month, no significant macroscopic changes were observed in the skin of young mice (Fig. 6B), but an increase in epidermal thickness was observed (Fig. 6C, $p < 0.05$), with similar changes to the eczema, such as hyperkeratosis and parakeratosis, which may be a benign response of EpiSCs to AA-induced inflammation. On the contrary, the skin of middle-aged mice showed flaky desquamation, but there was no statistical difference in epidermal thickness ($p > 0.05$).

Further experiments revealed that one-month AA feeding did not affect GPX4 expression levels in the epidermis of young or middle-aged mice (Fig. 6D, Fig. S5, $p > 0.05$). As for the epidermis of young mice, AA feeding did not significantly affect the AA and MDA content (Fig. 6E and F, $p > 0.05$), but did lead to decreased GSH levels (Fig. 6G, $p < 0.01$) and an increase in the lipid peroxidation product 4-HNE (Fig. 6H, $p < 0.01$). In contrast, for the epidermis of the middle-aged mice, AA feeding significantly increased the AA content ($p < 0.01$), accompanied by a decrease in GSH ($p < 0.01$), as well as a significant increase in MDA and 4-HNE levels ($p < 0.01$).

### 2.7. Se-Met rescued AA-induced ferroptosis in EpiSCs by promoting GPX4 expression

Considering the critical role of decreased GPX4 expression in the ferroptosis of EpiSCs in aged epidermis, we sought to explore

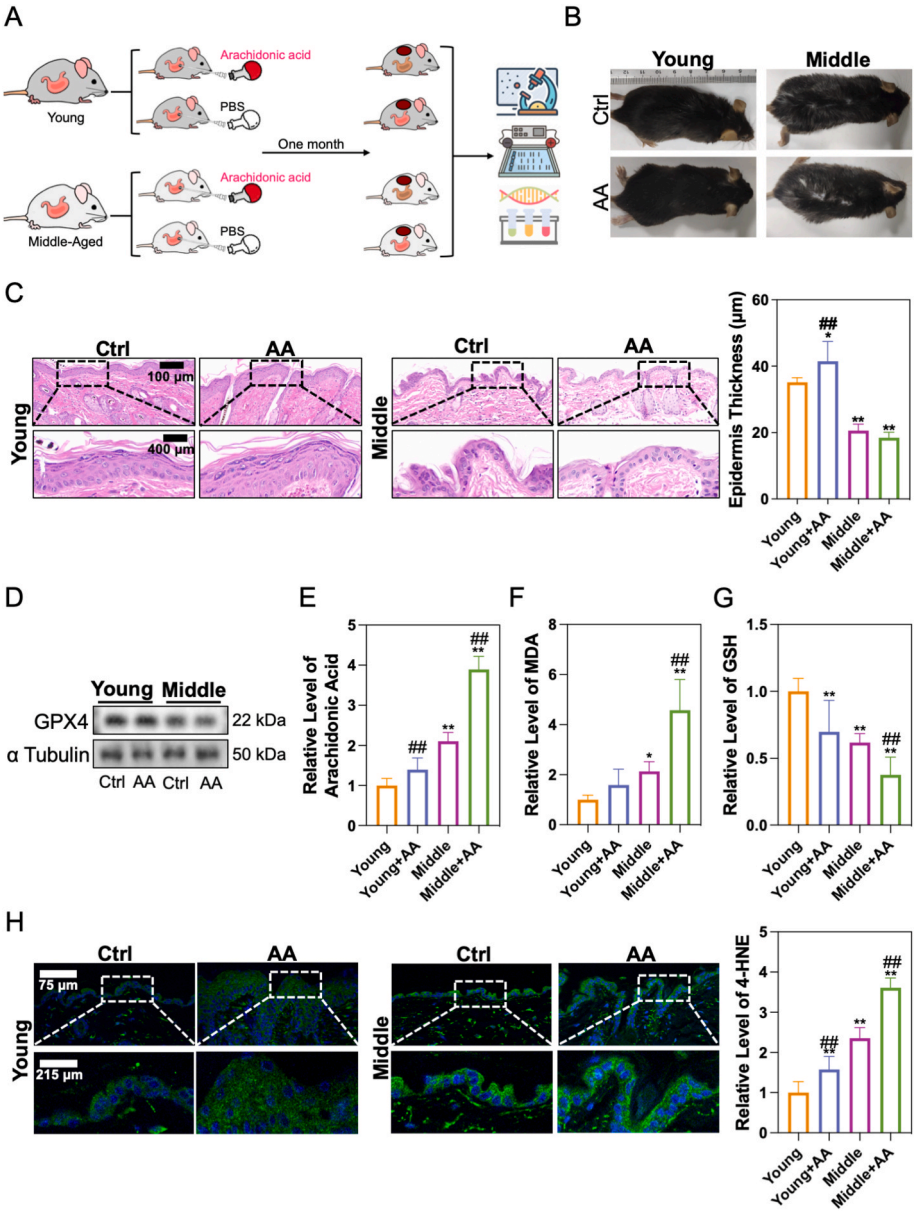


**Fig. 6.** Arachidonic acid feeding triggered ferroptosis in EpiSCs of middle-aged mice (A) To investigate the impact of additional AA and impaired GPX4 expression on the ferroptosis of EpiSCs at an in vivo level, experiments were conducted on middle-aged mice. After being orally challenged with AA for one month, the dorsal epidermis was collected for experiments. (B) Gross photographs of the skin from young and middle-aged mice fed with AA for one month. (C) Skin tissues were exposed to HE staining to explore changes in the structure of the epidermal layer. The box area adjacent to each photograph shows an enlarged version of the black square. N = 6. Scale bar, 100 μm and 400 μm $^{*}p < 0.05$, $^{**}p < 0.01$, versus the young group. $^{\#\#}p < 0.01$ versus the middle-aged group. (D) Western Blot was used to detect changes in GPX4 expression levels. N = 6. (E)–(G) The AA (E), MDA (F) and GSH (G) content in the epidermis was measured. N = 6. $^{*}p < 0.05$, $^{**}p < 0.01$, versus the young group. $^{\#\#}p < 0.01$ versus the middle-aged group. (H) Immunofluorescence staining was used to label lipid peroxidation products in the skin with antibodies against 4-HNE. N = 6. Scale bar, 75 μm and 215 μm $^{**}p < 0.01$, versus the young group. $^{\#\#}p < 0.01$ versus the middle-aged group.

therapeutic measures that could promote GPX4 expression. Selenium is a cofactor for the human antioxidant system including SOD and glutathione [27,28]. Already developed as a dietary supplement for improving thyroid and cardiovascular function, Se-Met has been shown to promote GPX4 expression by providing Se [29]. The CCK-8 assay demonstrated that incubating EpiSCs with Se-Met across a wide concentration range from 1.25 μM to 160 μM for 24 h resulted in no significant cytotoxic effects on the cells (Fig. S6). Thus, in vitro experiments, we supplemented AA-exposed *siGPX4* EpiSCs with 5 μM Se-Met, to investigate its potential protective effect on ferroptosis, with the ferroptosis inhibitor Fer-1 used as a positive control. With additional supplementation of Se-Met, the GPX4 expression in *siGPX4* EpiSCs increased (Fig. 7A, $p < 0.05$), accompanied by an increase in cell survival indicated by the CCK-8 assay (Fig. 7B, $p < 0.01$), similar to the Fer-1 group. Furthermore, the exposure of AA-incubated *siGPX4* EpiSCs to Se-Met resulted in a notable amelioration in MDA content and GSH levels, paralleling the outcomes achieved with Fer-1 treatment (Fig. 7C and D). The lipid peroxidation assay revealed Se-Met's potent inhibitory action on AA-induced ferroptosis, reflecting an efficacy comparable to that observed with Fer-1 (Fig. 7E, $p < 0.01$).

### 2.8. The synthesis and characterization of AC-PEG-Se-Met

After preliminary in vitro experiments confirmed the protective effect of Se-Met against AA-induced ferroptosis of GPX4-deficient EpiSCs, we further explored the delivery and application of Se-Met to attenuate skin aging. Hydrogels can facilitate the prolonged retention of drugs on the skin and wound surfaces through controlled release [30,31]. Moreover, compared with gauze or absorbent dressings with fixed shape, hydrogels can better adapt to various anatomical sites of skin and wound surfaces [32]. With excellent biocompatibility and biosafety, GelMA is a photopolymerizable hydrogel generated from modified natural extracellular matrix components, making it a potential material for tissue repair [33]. Besides, GelMA is resistant to degradation by proteolytic enzymes such as gelatinase and collagenases, endeavoring it the prerequisites for the application in wound healing and photoprotection [34].

Considering that the direct use of GelMA for drug delivery may lead to rapid drug release, we modified Se-Met using acrylate-functionalized polyethylene glycol N-hydroxysuccinimide ester (AC-PEG-NHS) tethers to achieve covalent immobilization within GelMA hydrogels (Fig. 8A). The acrylate groups in the AC-PEG-NHS participate in the formation of photopolymerizable double-bonded hydrogel networks, while the NHS esters react with the amino groups (-NH2) of Se-Met to form stable amide bonds. This approach aimed at extending the release period and preventing burst release of drugs.

The MALDI-ToF results reveal distinct bands and molecular weight shifts corresponding to the synthesized conjugates (Fig. 8B). The X-ray Photoelectron Spectroscopy (XPS) analysis of AC-PEG-Se-Met demonstrated the presence of the characteristic elemental peak of Se 3d, confirming the existence of selenium in the synthesized product (Fig. 8C). The high-resolution C 1s XPS spectrum (Fig. 8D) of AC-PEG-Se-Met reveals four distinct peaks: C–C bonding at 284.86 eV, C–O bonding at 286.15 eV, O═C–*O*- bonding at 288.88 eV, and O═C–NH bonding at 288.1 eV. Similarly, the O 1s high-resolution XPS spectrum shows peaks at C–O (533.2 eV), C═O (532.25 eV), and O═C–NH (531.43 eV). The presence of the O═C–NH peak in both C 1s and O 1s spectra indicates the formation of amide bonds in AC-PEG-Se-Met. Furthermore, the N 1s high-resolution XPS spectrum exhibits a peak at 399.75 eV, consistent with the amide bond. Additionally, the presence of two peaks in the Se

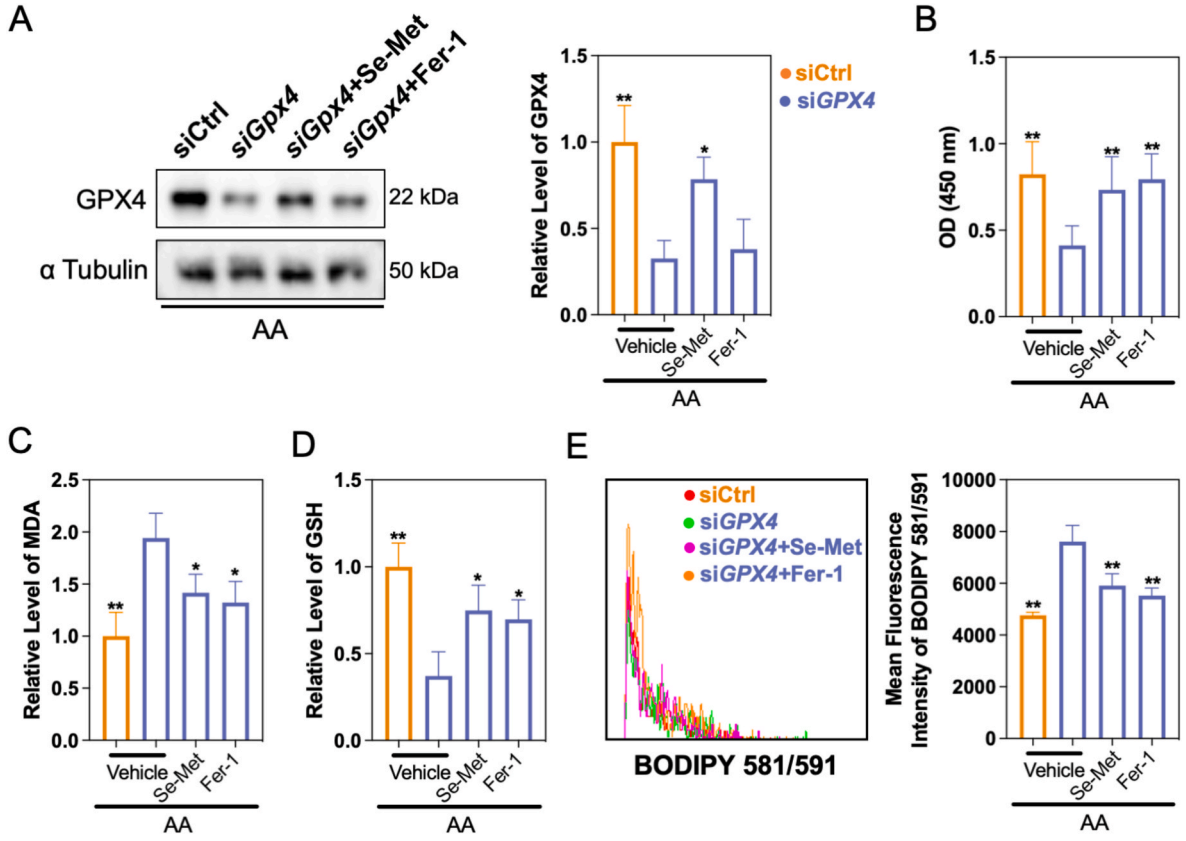


**Fig. 7.** Se-Met rescues GPX4-deficient EpiSCs from ferroptosis under arachidonic acid stimulation (A) Western Blot analysis was performed to investigate the effect of Se-Met exposure on GPX4 expression in GPX4-deficient EpiSCs. N = 3. *$p < 0.05$, **$p < 0.01$, versus the *siGpx4* group with vehicle exposure. (B)–(E) The impact of Se-Met on cell viability (B), MDA content (C), GSH content (D), and levels of lipid peroxidation products labeled by BODIPY 581/591 (E) in GPX4-deficient EpiSCs exposed to AA. N = 3. *$p < 0.05$, **$p < 0.01$, versus the *siGpx4* group with vehicle exposure.

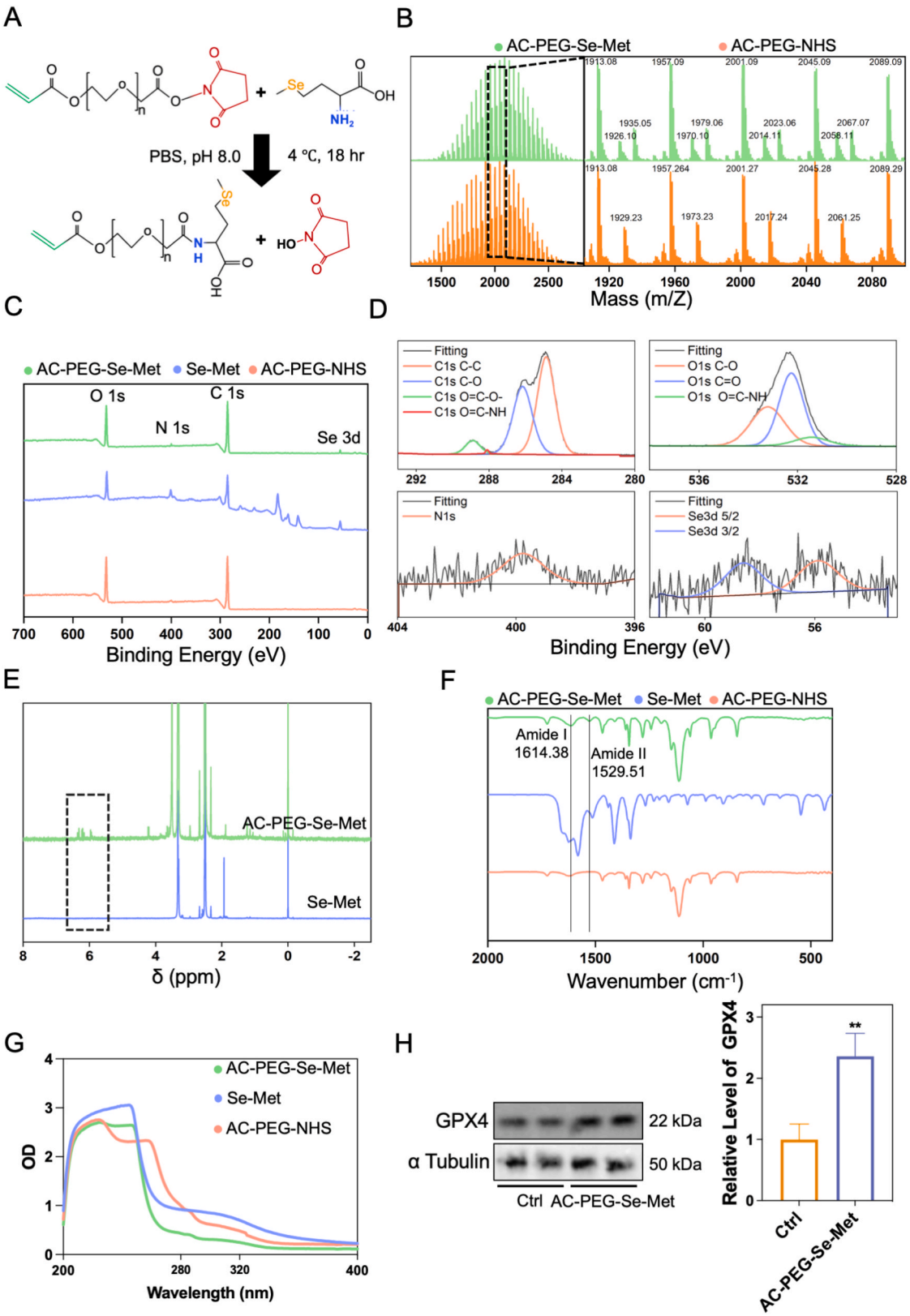


**Fig. 8.** The characterization of AC-PEG-Se-Met (A) Schematic representation of the covalent crosslinking process of AC-PEG-NHS and Se-Met. (B) MALDI-ToF mass spectrometry analysis. (C) XPS survey spectra. (D) High-resolution XPS spectrum. (E) $^{1}$H NMR analysis was employed to detect the characteristic double bonds of the product following covalent conjugation, indicated by a black dashed line. (F) FTIR spectra. (G) UV–Vis absorption spectra in the ultraviolet region. (H) AC-PEG-Se-Met was used to incubate human primary EpiSCs for 48 h, and changes in GPX4 levels were detected by Western Blot. N = 3. $^{**}p < 0.01$ compared to the control group.

3d high-resolution XPS spectrum, 3d 5/2 at 55.88 eV and 3d 3/2 at 58.6 eV, further confirms the effective covalent linkage of Se-Met with AC-PEG-NHS.

Nuclear magnetic resonance (NMR) hydrogen spectroscopy further corroborated the successful covalent grafting of AC-PEG-NHS and Se-Met, as evidenced by the emergence of characteristic double-bond peaks near 6 ppm (indicated by the black dashed line) in the AC-PEG-Se-Met spectrum (Fig. 8E). In Fourier-Transform Infrared Spectroscopy (FTIR) spectra, AC-PEG-Se-Met exhibits amide I and II peaks at 1614.38 and 1529.51 $cm^{-1}$, signifying the successful establishment of amide bonds (Fig. 8F). But AC-PEG-NHS only shows a single C═O peak at 1620.17 $cm^{-1}$ in this region. In the UV–Vis absorption spectra (Fig. 8G), Se-Met exhibited a distinct peak at 245.5 nm, which was altered upon its conjugation with AC-PEG-NHS, indicative of a successful covalent bonding. Furthermore, both Se-Met and AC-PEG-Se-Met showed substantial UV absorption in the spectral range corresponding to that of UV-induced skin damage. This absorption profile suggests a potential utility of these compounds in the prevention of photoaging, wherein they could

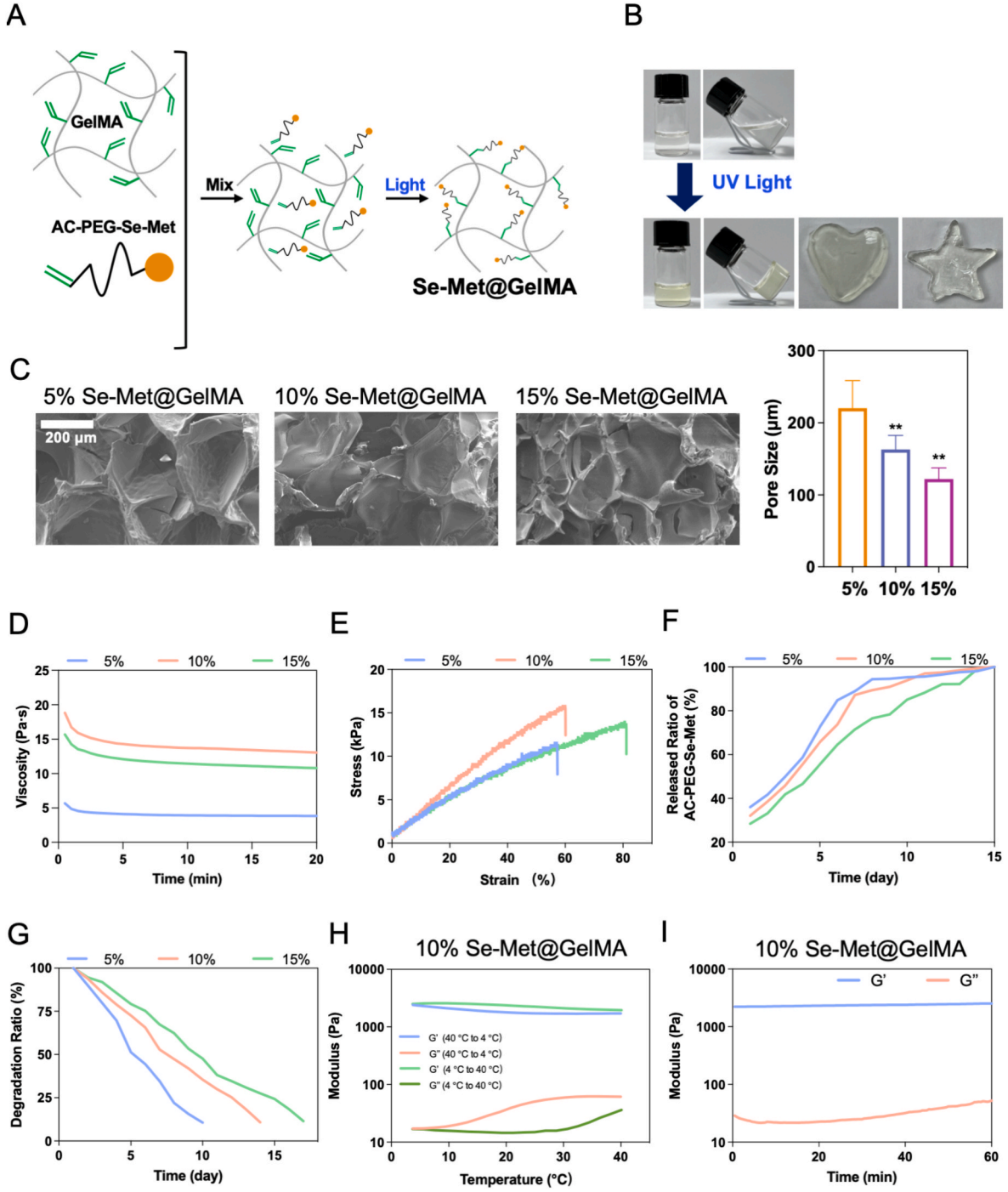


**Fig. 9.** The characterization of Se-Met@GelMA hydrogel (A) Schematic representation of the synthesis process of Se-Met@GelMA hydrogel. (B) Schematic illustration of the photo-crosslinking process of Se-Met@GelMA hydrogel. (C) SEM images of different concentrations of GelMA loaded with 5 μM AC-PEG-Se-Met, with the mean pore size calculated. Scale bar = 200 μm. N = 6. $^{**}p < 0.01$ compared to 5% Se-Met@GelMA group. (D)–(G) Viscosity curve (D), stress-strain curve (E), the sustainable release ratio (F) and the degradation ratio (G) of Se-Met@GelMA hydrogel over time. (H), (I) Modulus change curves of 10% Se-Met@GelMA hydrogel with temperature and time.

act as a molecular shield against UV radiation.

AC-PEG-Se-Met, at concentrations ranging from 1.25 μM to 160 μM, was co-cultured with EpiSCs for 24 h, revealing no significant cytotoxicity (Fig. S7). Importantly, AC-PEG-Se-Met retained the native bioactivity of Se-Met, indicated by its promotion of GPX4 expression in EpiSCs (Fig. 8H, $p < 0.01$).

### 2.9. The synthesis and characterization of Se-Met@GelMA hydrogel

GelMA was synthesized by the direct reaction of gelatin with methacrylic anhydride (MA) in phosphate buffer at 50 °C, introducing methacryloyl substitution groups on the reactive amine and hydroxyl groups of the amino acid residues. It is worth noting that the chemical modification of gelatin by MA typically involves less than 5% of the amino acid residues in the molar ratio, indicating that most of the functional amino acid motifs remain intact. Lithium Phenyl(2,4,6-trimethylbenzoyl)phosphinate (LAP) was added to enable the hydrogels to be crosslinked by UV light. Here, GelMA with an MA substitution degree of 60% was chosen for further investigation. AC-PEG-Se-Met was incorporated into different concentrations of GelMA (5%, 10% and 15%) to explore a more suitable drug delivery system (Fig. 9A). Following UV-induced photo-crosslinking, the Se-Met@GelMA hydrogel can be molded into any desired shape (Fig. 9B). The porous structures of Se-Met@GelMA hydrogels were observed via scanning electron microscope (SEM, Fig. 9C). The surface morphology of the hydrogels exhibited a smooth, continuous, and interconnected porous three-dimensional network structure. The 5%, 10%, and 15% Se-Met@GelMA hydrogels respectively had a pore size of 220.3 μm, 163.2 μm, and 122.2 μm with the difference being statistically significant.

To address the irregular shape of skin, self-healing hydrogels are preferred. Thus, a rotational shear test was performed on the crosslinked Se-Met@GelMA hydrogels at a shear rate of 10 τ/s to obtain a profile of viscosity versus time (Fig. 9D), and the 10% Se-Met@GelMA hydrogel had the highest viscosity. Additionally, the elongation at break for 5%, 10%, and 15% Se-Met@GelMA hydrogels were 57.33%, 60.05%, and 81.16% respectively, with corresponding tensile strengths of 10.42, 15.46, and 13.67 kPa (Fig. 9E).

We immersed the manufactured Se-Met@GelMA hydrogel in PBS, with the concentration of the released AC-PEG-Se-Met measured at predetermined time points (Fig. 9F). Se-Met@GelMA hydrogel of the three concentrations all exhibited relatively sustained release rates during the initial days, and the pinnacle of drug release occurred around day 5 and lasted for approximately 3 days. Drug release of the 5% and 10% hydrogels reached 95% respectively at day 10 and 11, while the 15% hydrogel at day 14. After being immersed in the culture medium, the degradation rate of hydrogels was measured every 2 days (Fig. 9G). 10% and 15% Se-Met@GelMA hydrogels degraded much slower than the 5% hydrogel.

The temperature-dependent modulus changes were studied to verify the constant self-assembly of the hydrogels after their formation, by analyzing the changes in the storage modulus (G′) and loss modulus (G″) (Fig. 9H, Fig. S8A). The results showed that the cross-linked 10% Se-Met@GelMA hydrogel remained solid at ambient temperatures of 4–40 °C under 1% strain and 5 Hz frequency. As the temperature increased from 4 °C to 40 °C, G′ decreased from 2499.4 Pa to 1960.3 Pa, and G″ increased from 16.98 Pa to 36.16 Pa. Conversely, as the temperature reduced from 40 °C to 4 °C, G′ increased from 1715.7 Pa to 2404.7 Pa, and G″ decreased from 61.64 Pa to 17.26 Pa. Time-dependent modulus assessments were conducted to ascertain the stability of the hydrogels post-formation (Fig. 9I, Fig. S8B). It was observed that 10% Se-Met@GelMA hydrogel exhibited a notably higher modulus compared to the 5% hydrogel, indicating enhanced mechanical properties. Additionally, 10% hydrogels demonstrated superior stability relative to those with a 15% concentration, suggesting an optimal balance of structural integrity and durability at the 10% concentration level.

Water retention capability is considered a crucial parameter for hydrogels as medical dressings, as it provides an appropriate microenvironment for wound healing. When fully hydrated, 10% Se-Met@GelMA was able to absorb 595.04% of its own weight in water, slightly higher than the 553.43% observed for 10% GelMA hydrogel (Fig. S8C). Over time, the water content of Se-Met@GelMA remained consistently higher than that of the GelMA group, with statistical significance at 24 and 36 h ($p < 0.05$). This indicates that the incorporation of AC-PEG-Se-Met into hydrogels can enhance the water absorption and retention properties of the hydrogel, facilitating the absorption of wound exudate and maintaining the necessary moist environment for wound healing.

Investigating the cytotoxicity of hydrogels with varying GelMA and AC-PEG-Se-Met concentrations revealed no significant cell toxicity on EpiSCs over 24 h (Fig. S8D). After incubating with 2% SD rat red blood cells for 3 h, hydrogels with varying GelMA and AC-PEG-Se-Met concentrations, maintained cellular integrity with the maximal hemolytic activity not exceeding 1% (Fig. S8E). In contrast, the positive control group, when exposed to Triton X-100, exhibited complete erythrocyte lysis, culminating in a hemolysis rate of 100%.

### 2.10. Se-Met@GelMA hydrogel accelerated wound healing in aged mice

10% Se-Met@GelMA hydrogel was employed to evaluate its effect on wound healing in aged skin via a full-thickness skin defect model (Fig. 10A). The old mice were randomly divided into four groups and respectively treated with PBS (Ctrl group), 10% GelMA (GelMA group), AC-PEG-Se-Met (Se-Met group), and 10% Se-Met@GelMA (Se-Met@GelMA group). Digital photographs were taken on Day 0, 4, 7, 10, and 14 after injury (Fig. 10B). The Se-Met@GelMA group had the fastest wound healing rate, followed by the GelMA and the Se-Met group at any predetermined time point (Fig. 10C and D). On Day 14, wounds in the Se-Met@GelMA group had completely healed, while the other three groups were observed with incomplete healing.

To further evaluate the healing potential of Se-Met@GelMA hydrogel, HE and MASSON staining were conducted on Day 14 (Fig. 10E and F). The skin of the wound margin was magnified to better showcase the tissue morphology. Briefly, the Se-Met@GelMA group had a continuous epidermal layer (Fig. 10E), which was much more inclined towards normal epidermal structure compared to the other three groups. Meanwhile, the infiltrated inflammatory cells in the dermis of the Se-Met@GelMA group were less numerous than those in the other groups, indicating a more stable internal environment that favored wound healing. Correspondingly, the Se-Met@GelMA group showed a significant increase in the thickness of neoepithelium (Fig. S9A). The collagen fibers in the Se-Met@GelMA group were arranged in a more orderly manner with a higher level of maturity, indicating a better quality of healing (Fig. 10F). The content of collagen fibers within the dermis treated with Se-Met@GelMA was 1.64 times greater than that of the control group (Fig. S9B). This indicates that the Se-Met released gradually from the hydrogel notably enhances collagen synthesis in aged dermal fibroblasts.

In vivo ferroptosis levels were assessed on Day 14 to explore the therapeutic mechanism of Se-Met@GelMA. The Se-Met@GelMA group exhibited higher GPX4 expression and lower 4-HNE levels in the neoepithelium than the other groups (Fig. 11A and B, Figs. S9C and S9D). Correspondingly, the Se-Met@GelMA group showed a significant increase in GSH content (Fig. 11C), and decrease in MDA, AA and PGE2 content (Fig. 11D–F), consistent with the improvement in GPX4 expression.

On Day 14, biochemical analyses of mouse blood revealed no significant alterations in liver and kidney function biomarkers across all groups (Fig. S9E). Furthermore, HE staining showed that the cellular structure and morphology of the heart, liver, spleen, lungs, and kidneys in mice from the Se-Met@GelMA group remained unchanged, comparable to those in the Ctrl group (Fig. S9F). These findings collectively affirm the exceptional biocompatibility of Se-Met@GelMA for wound

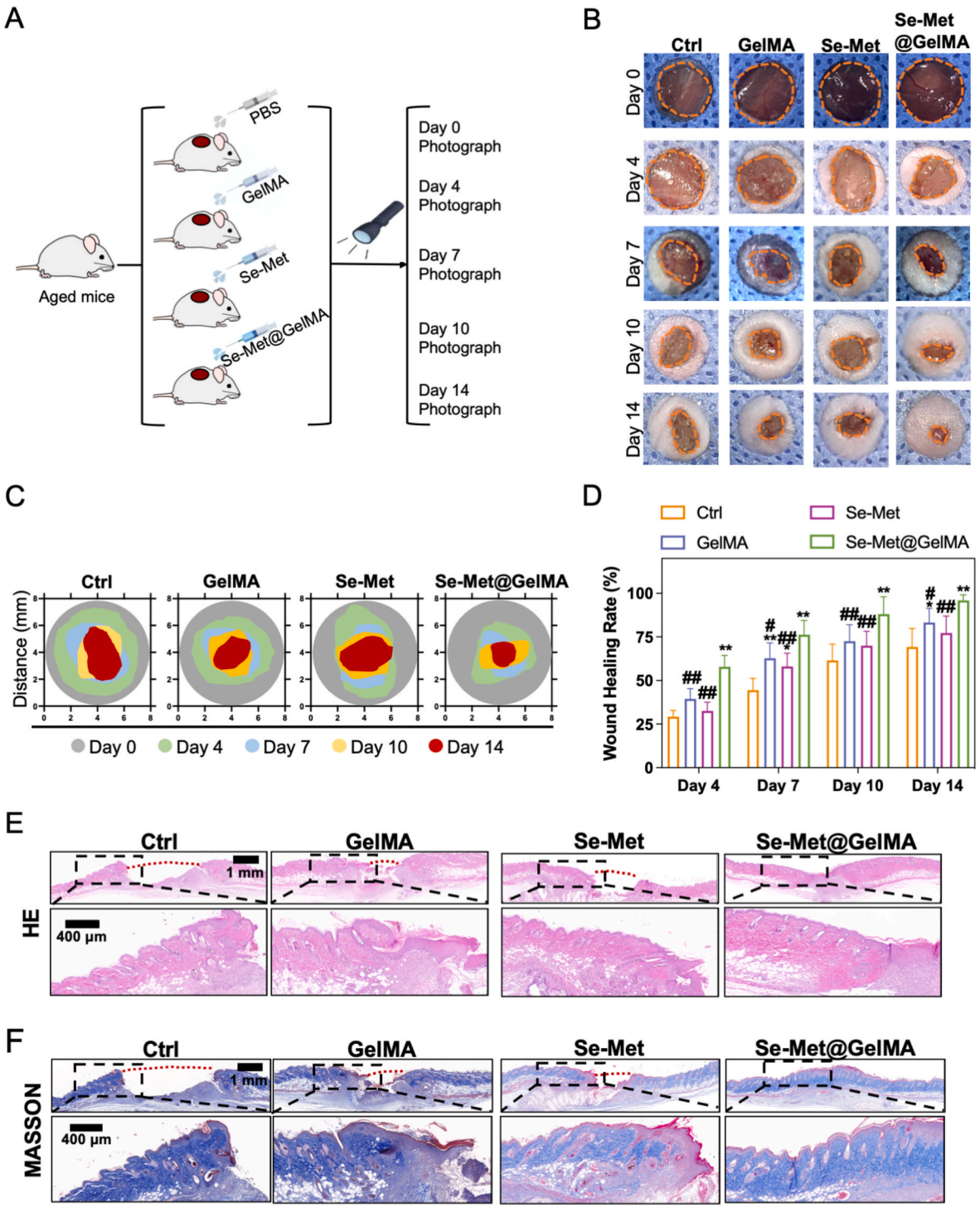


**Fig. 10.** Se-Met@GelMA hydrogel accelerated wound healing in aged mice (A) Schematic diagram representing the experimental procedure of the full-thickness skin defect model in aged mice. (B) Representative macroscopic illustration of wound healing at indicated days. (C) The schematic photographs of wound area during 14 days. (D) Quantitative analysis of wound healing rate. N = 8. $^{*}p < 0.05$, $^{**}p < 0.01$ versus Ctrl group. $^{\#}p < 0.05$, $^{\#\#}p < 0.01$ versus Se-Met@GelMA group. (E) HE stained sections of each group at Day 14 showing morphometric analysis of wound width (indicated by the red dotted line) and the newly formed epithelium (enlarged and displayed within a black box). N = 6. Scale bar, 1 mm or 400 μm. (F) MASSON staining showing the levels of collagen deposition at Day 14. The box area adjacent to each photographs shows an enlarged version of the black square. The red dotted line indicated the width of the remained wound. N = 6. Scale bar, 1 mm or 400 μm.

healing in aged mice, underscoring its promising potential for clinical applications in tissue repair and regeneration.

### *2.11. Se-Met@GelMA hydrogel exhibits photoprotective effects in the photoaging mice*

Further, we explored the photoprotective effects of Se-Met@GelMA through a UV-induced photoaging model in BALB/c-nu mice

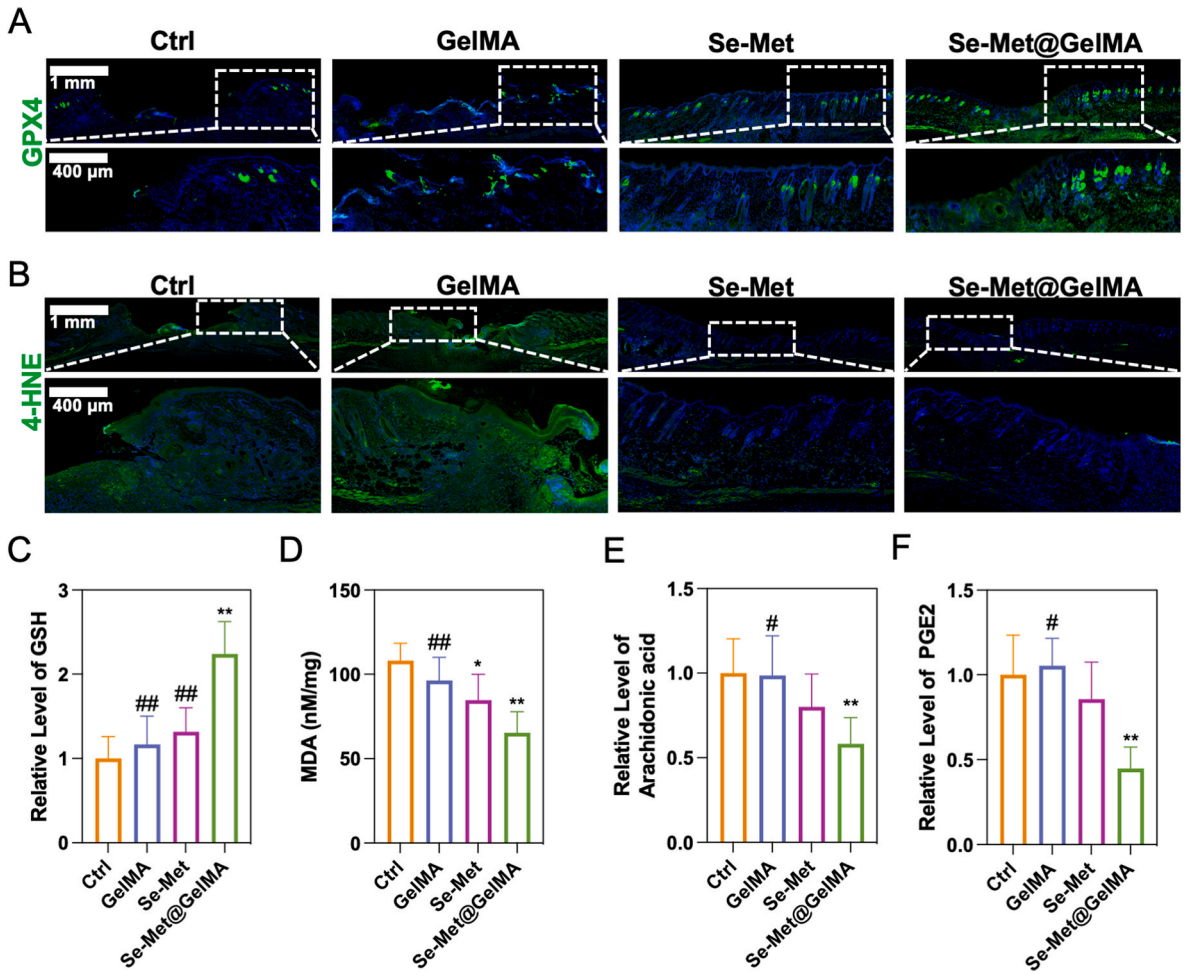


**Fig. 11.** Se-Met@GelMA hydrogel inhibited ferroptosis in aged mice (A), (B) Immunofluorescence staining was performed to label GPX4 and 4-HNE in peri-wound tissues at Day 14. The boxed area adjacent to each photograph shows an enlarged version of the white square. N = 6. Scale bar, 1 mm or 400 μm. (C)–(F) On Day 14, newly formed epidermis from each group was collected and assessed for the content of GSH (C), MDA (D), AA (E), and PGE2 (F). N = 6. $^{*}p < 0.05$, $^{**}p < 0.01$ versus Ctrl group. $^{\#}p < 0.05$, $^{\#\#}p < 0.01$ versus Se-Met@GelMA group.

(Fig. 12A). Post-cumulative UVB irradiation, the dorsal skin of mice exhibited typical signs of photodamage, including pronounced erythema, scaling, thickening, and a leathery texture (Fig. 12B and C). The Se-Met@GelMA hydrogel displayed a concentration-dependent attenuation of skin photodamage, evidenced by a significant decrease in erythematous areas and scale formation (Fig. 12C).

Photoaging is associated with an upregulation of matrix metalloproteinases, including MMP1 and MMP9, which can lead to the disruption of normal barrier function [35]. This disruption is evident as an increase in Transepidermal Water Loss (TEWL). Meanwhile, UVB radiation could induce an enhanced inflammatory response through the release of cytokines and neuroactive mediators such as IL-6 and CCL8 [35]. This, in turn, promotes continual proliferation of EpiSCs, manifesting as an increase in epidermal thickness. The group treated with the highest concentration of Se-Met@GelMA (2Se-Met@GelMA) showed the lowest TEWL and skin thickness among all UVB-irradiated groups (Fig. 12D, Fig. S10A), indicating the inhibited inflammatory response and the restoration of skin barrier function.

HE staining (Fig. 12E) revealed that UVB-exposed skin underwent characteristic photodamage changes. The epidermis exhibited substantial irregular thickening, with four to eight layers of keratinocytes, with signs of disorganized cellular arrangement, nuclear condensation and deformation. Additionally, there was a disruption of the normal architecture of EpiSCs, aligning in a chaotic manner along the basement membrane. Concurrently, the dermal collagen fiber structure appeared disorganized and homogenized (Fig. 12F), and Elastin van Gieson (EVG) staining demonstrated disarranged and degenerated elastic fibers (Fig. 12G). Different concentrations of Se-Met@GelMA hydrogel ameliorated overall skin damage, with 2Se-Met@GelMA exhibiting the most potent protective effect against photodamage. The epidermal layer in the 2Se-Met@GelMA-treated mice was significantly thinner, showing a cell arrangement and morphology more akin to normal EpiSCs, particularly in terms of the more regular nuclear structure (Fig. 12E). In the dermis, collagen fiber bundles were neatly arranged and evenly distributed, with observable gaps between the fibers (Fig. 12F), and most elastic fibers maintained a clear structure and normal morphology (Fig. 12G). These histopathological differences underscore the superior photoprotective efficacy of 2Se-Met@GelMA against UVB-induced skin damage.

Further, staining for ferroptosis revealed that Se–Me@GelMA presents a concentration-dependent amelioration in lipid peroxidation levels in UV-exposed skin, as evidenced by the gradual increase in GPX4 and decrease in 4-HNE expression (Fig. 13A–D). ELISA assays confirmed an increase in GSH post-treatment with 2Se-Met@GelMA (Fig. 13E), along with a decrease in the expression of MDA (Fig. 13F), AA (Fig. S10B), and PGE2 (Fig. S10C).

Previous research has established the role of DNA damage and inflammatory responses, induced by UV radiation, in the process of photoaging and its contribution to the degenerative changes in skin [36,37]. In the GelMA group, UV exposure markedly induced DNA

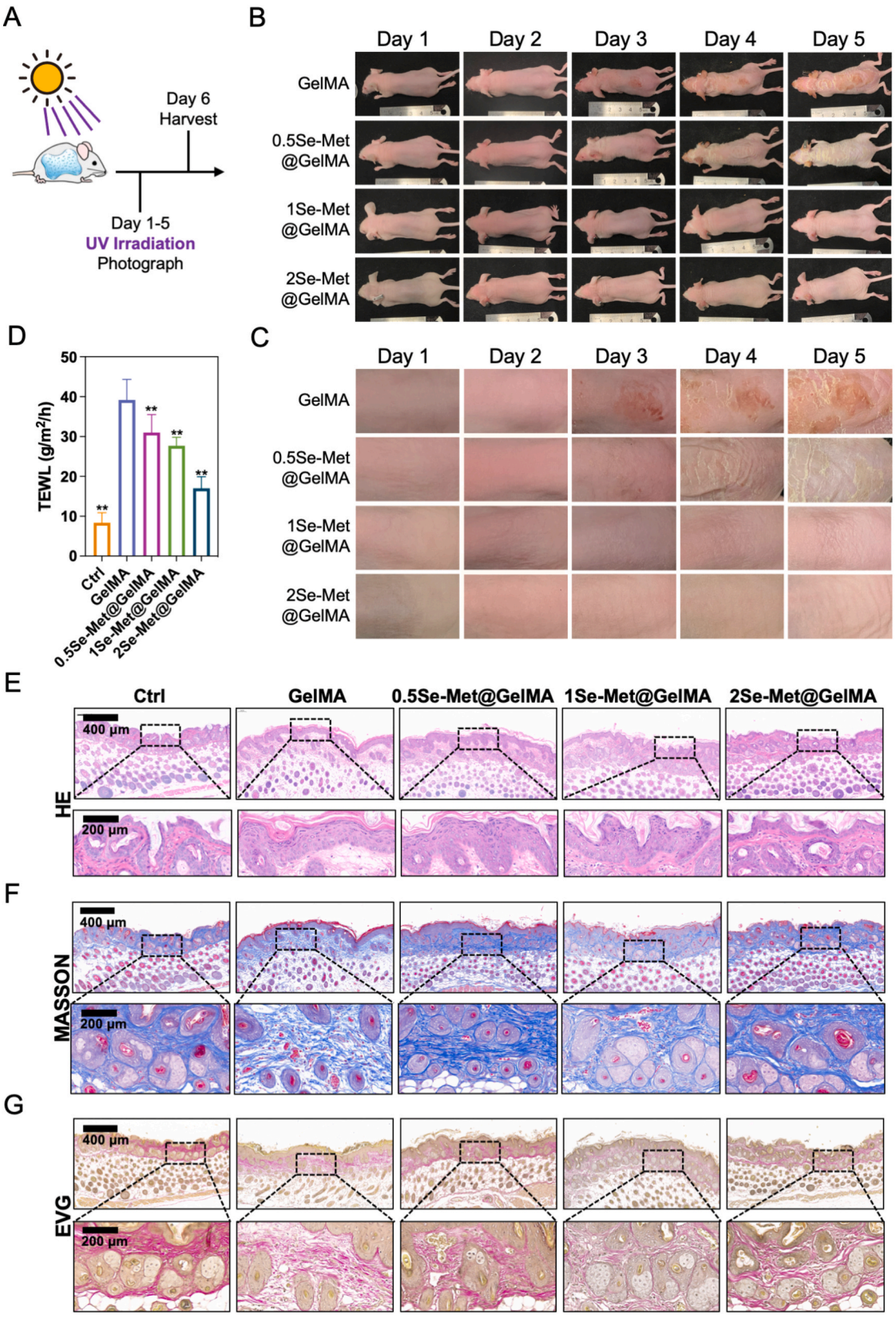


**Fig. 12.** Photoprotective effect of Se-Met@GelMA hydrogel on UV-exposed mice (A) Schematic diagram of the experimental procedure to validate the photoprotective efficacy of Se-Met@GelMA hydrogel in a photoaging model. (B), (C) Gross Morphology of the dorsal skin of UV-exposed mice (B) with an enlarged schematic representation (C). (D) Changes in TEWL in mice after 5 days of UV irradiation. $^{**}p < 0.01$ versus GelMA group. (E)–(G) Skin samples from mice exposed to 5 days of UV irradiation were utilized for HE staining (E), MASSON staining (F), and EVG staining (G). Each photograph is accompanied by an enlarged view of the area highlighted in the black square. Scale bar, 400 μm or 200 μm.

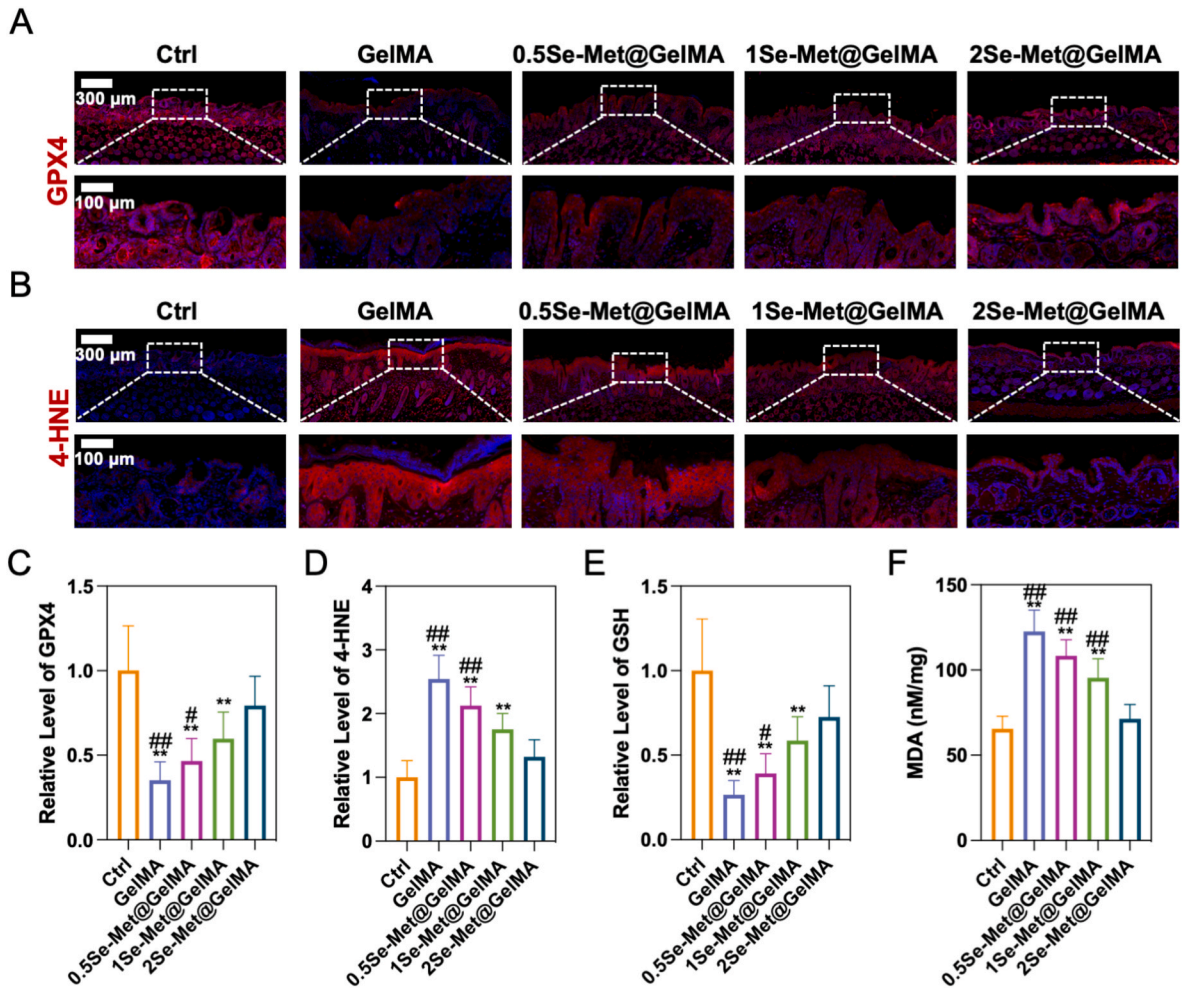


**Fig. 13.** The mechanism of the photoprotective effect of Se-Met@GelMA hydrogel (A)–(D) Immunofluorescence staining for GPX4 and 4-HNE in skin samples from mice post 5 days of UV irradiation. N = 6. $^{**}p < 0.01$ versus Ctrl group; $^{\#}p < 0.05$, $^{\#\#}p < 0.01$ versus 2Se-Met@GelMA group. Scale bar, 300 μm or 100 μm. (E), (F) Epidermis samples of mice after 5 days of UV exposure were harvested and analyzed for the levels of GSH (E) and MDA (F). N = 6. $^{**}p < 0.01$ versus Ctrl group; $^{\#}p < 0.05$, $^{\#\#}p < 0.01$ versus 2Se-Met@GelMA group.

damage-related marker λH2AX, along with an accumulation of inflammatory cytokines IL-6 and TNF-α, primarily enriched in the epidermis and hair follicles (Fig. 14A, Figs. S10D–S10F). However, 2Se-Met@GelMA hydrogel significantly ameliorated the expression of λH2AX and the release of inflammatory factors.

Matrix metalloproteinases (MMPs), which are extracellular matrix remodeling enzymes induced by UV in the photoaging process, accelerate the degradation of the extracellular matrix [38]. This degradation can lead to the loss of normal skin structure and functional impairment. Notably, 2Se-Met@GelMA hydrogel inhibited the expression of MMP1 and MMP9 in the epidermis after UV irradiation (Fig. 14B). This inhibition aligns with the more orderly arrangement of collagen observed in MASSON staining and higher elastic fibers in EVG staining in the 2Se–Me@GelMA group. On Day 6, biochemical analyses of mouse blood and HE staining of the organs confirmed the excellent biocompatibility of 2Se-Met@GelMA (Figs. S10G and S10H).

## 3. Discussion

Owing to the unique 3D network structure with high aqueous content and functional properties, emerging hydrogels are considered as the most promising candidates for tissue repair and organ regeneration, applicable in the repair of skin injuries, skull defect, cartilage injury, and arthritis domains [39,40]. The development of biocompatible materials is steering towards enhanced functionalities, encompassing tunable physicochemical properties, the aptitude to precisely conform to irregular defect geometries, and the advanced capability for the targeted, stimulus-responsive release of drugs, triggered by a variety of environmental cues such as pH, ROS, temperature, redox conditions, enzymatic activity, light, and magnetic fields [41,42]. Utilizing a unique composition of ROS-cleavable thioketal (TK) linkers and UV-responsive norbornene (NB) groups, Prof. Su et al. have developed the synthesis of an innovative factor-free hydrogel, engineered via a UV crosslinking-mediated gelation approach [43]. This hydrogel exhibits exceptional ROS scavenging functionality and a responsive degradation profile, meticulously designed to substantially augment the regenerative process in diabetic bone defects. Integrating multi-omics data analysis can provide precise therapeutic targets for the design of hydrogels, to address the dual challenges of delayed wound healing in elderly skin and the complexities of photoaging. In our study, transcriptomic and metabolomic analyses have uncovered a deteriorating microenvironment in aging EpiSCs, marked by an increase in the pro-inflammatory mediator AA and a decrease in the anti-inflammatory mediator GPX4. These changes contribute to enhanced lipid peroxidation and ferroptosis in EpiSCs. To address these characteristic alterations in aging EpiSCs, we developed the Se-Met@GalMA hydrogel, whose therapeutic efficacy was validated using a wound healing model in aged mice and a photoaging model.

Research into the role of metabolites in conditions such as aging, diabetes, and immune disorders has highlighted their significant impact

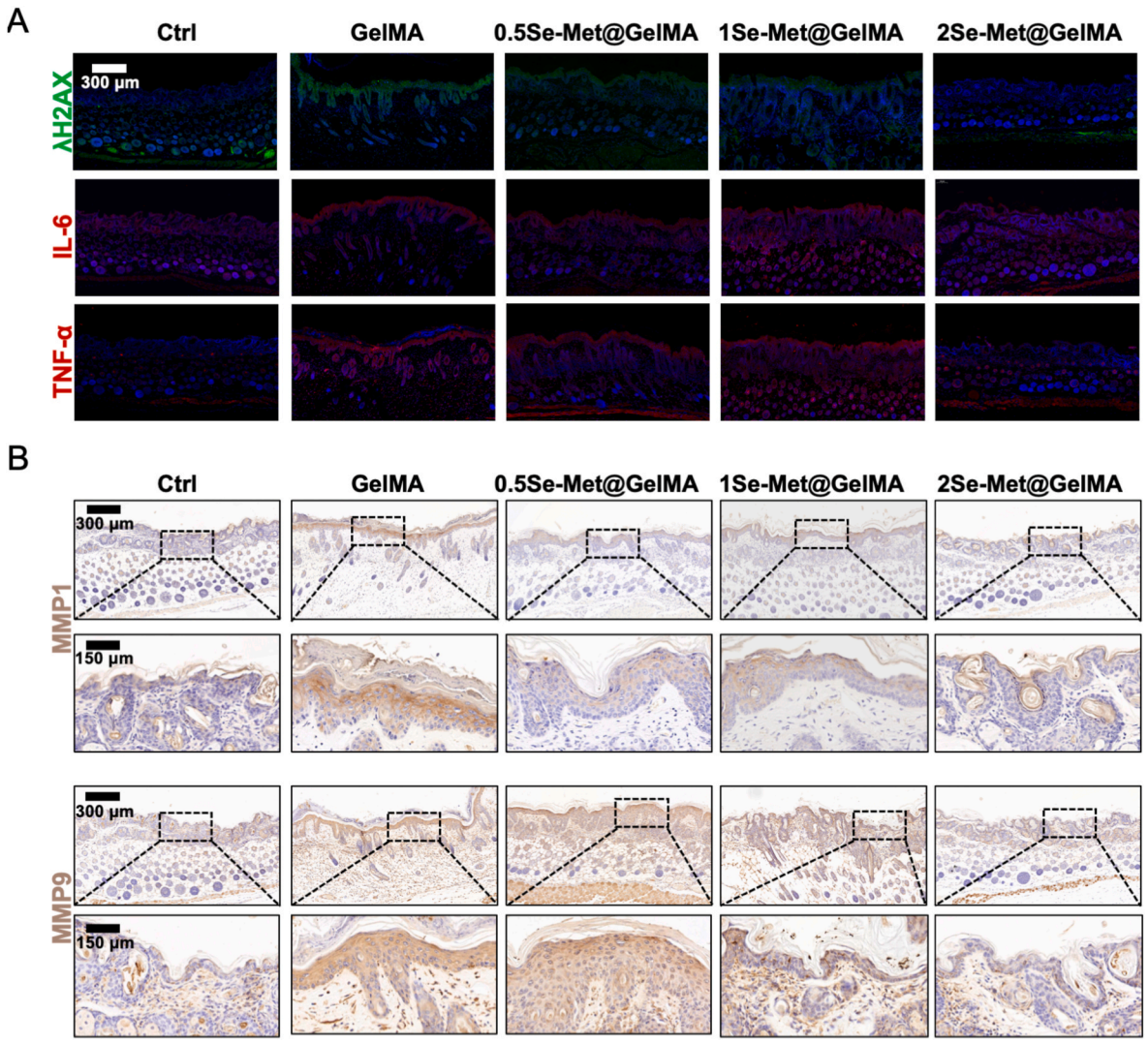


**Fig. 14.** The photoprotective effect of Se-Met@GelMA hydrogel on DNA damage and inflammation (A) Skin samples after 5 days of UV exposure were employed to evaluate the expression levels of the DNA damage marker λH2AX and the inflammatory factors IL-6 and TNF-α. N = 6. Scale bar, 300 μm. (B) Following 5 days of UV exposure, skin samples were analyzed to determine the expression levels of MMP1 and MMP9. N = 6. Scale bar, 300 μm or 150 μm.

[44]. In a metabolic analysis of diabetic foot ulcers, Tang et al. discovered a notable accumulation of phenylpyruvate which can be taken up by macrophages in a CD36-dependent manner, thereby enhancing palmitoylation of the NLRP3 protein [45]. This process leads to the activation of inflammasomes and the release of inflammatory cytokines, triggering an inflammatory phenotype in macrophages. Dietary restriction of phenylalanine can promote the healing of diabetic wounds. Studies have shown that AA induced the oxidation of unsaturated lipids in small intestinal epithelial cells by enhancing the inflammatory response, then triggered cell death through ferroptosis [25]. Moreover, AA has been shown to alleviate LPS-induced Kupffer cells pyroptosis by interacting with GPR120 to inhibiting the assembly of inflammasome complexes [46]. As for the skin, AA induces autophagy in the epidermis and stimulate collagen synthesis in the dermis [47]. Enhanced metabolism of AA has been shown to be associated with the exacerbation of atopic dermatitis [48]. In our study, we discovered that AA markedly instigated cell mortality in GPX4-deficient EpiSCs with a notable escalation in lipid peroxidation, a reduction in GSH levels, and substantial mitochondrial impairment. Dietary supplementation of AA could induce accumulation of AA in the epidermis and degenerative loss of EpiSCs, providing valuable guidance for dietary management in the clinical treatment of elderly patients with chronic wounds.

In the intricate process of tissue repair, numerous bioactive elements with exceptional stability such as zinc (Zn), calcium (Ca), copper (Cu), lithium (Li), silicon (Si), and silver (Ag), can be integrated into biomaterials [49]. These elements can induce progenitor cell differentiation or regulate immune responses through growth factor signaling pathways, orchestrate neuroregulation, stimulate angiogenesis, and promote osteogenesis. Selenium is an essential trace element and its insufficient intake may reduce the activity of GPXs. In the active site of GPXs, selenium is present in the form of selenocysteine, along with tryptophan, glutamine, and asparagine residue, forming the catalytic tetrad as a proton shuttle [50]. The selenocysteine undergoes a transformation between reduced and oxidized states, enabling GPXs to reduce hydrogen peroxide or lipid peroxides to $H_2O$ or the corresponding alcohols [51]. During this process, GPXs utilize GSH as an electron donor, converting it to oxidized glutathione (GSSG), thereby mitigating oxidative stress-induced cellular damage [52]. Selenium exists in two primary forms: inorganic and organic. Inorganic selenium, such as selenite and selenate, is predominantly absorbed by cells through passive diffusion or ion exchange mechanisms. Before being utilized in the synthesis of GPXs proteins, inorganic selenium requires a lengthy metabolic pathway. In contrast, organic forms of selenium, principally Se-MetSe-Met and selenocysteine, are absorbed via active amino acid transporters and can

be directly incorporated into proteins. This process rapidly replenishes the selenium necessary for catalytic functions without the need for complex transformation pathways. Additionally, organic selenium has been demonstrated to possess a higher safety profile compared to its inorganic counterpart [53]. Selenium supplementation has been shown to enhance GPX4 expression in T cells, increase the number of TFH cells, and promote the antibody response in adults after influenza vaccination [29]. As an FDA-approved organic selenium compound for use as a dietary supplement, Se-Met exhibits a strong protective role in combating oxidative stress. Se-Met supplementation has been shown to activate the NRF2/GPX4 pathway, reduce mitochondrial damage, enhance the activity of antioxidant enzymes, and alleviate ferroptosis induced by decabromodiphenyl ether-triggered oxidative stress in the chicken brain [54]. Furthermore, Se-Met has been demonstrated to protect the liver from dietary deoxynivalenol exposure via the Nrf2/PPARγ-GPX4-ferroptosis pathway in mice [55]. These examples underscore the vital role of Se-Met in resisting ferroptosis via the GPX4 pathway, highlighting its substantial potential for clinical applications. Our experiments have confirmed that the additional supplement of Se-Met to *siGPX4* EpiSCs could promote GPX4 expression with the cell survival rescued from AA exposure, and improve lipid peroxidation and GSH levels.

With Se-Met being as a candidate drug for targeted therapy of EpiSCs ferroptosis in aging skin, the major challenge was to optimize drug delivery to the epidermis. Due to its excellent biocompatibility, stability, and amphiphilicity, PEG has been approved by the FDA and is extensively utilized in the development of injectable hydrogels [39,56,57]. PEG-functionalized Se-Met was proved to retain the native bioactivity of Se-Met but could be stably incorporated and retained within the GelMA hydrogel over seven days, thus meeting the basic requirements for prolonged wound healing process and the photoprotection. Se-Met@GelMA hydrogel has been shown to effectively accelerate wound healing in chronological aging model with aged mice, by inhibiting lipid peroxidation and ferroptosis. Furthermore, in the photoaging model, this hydrogel also demonstrates significant efficacy in mitigating inflammation and lipid peroxidation in UV-exposed mice. The Se-Met@GelMA hydrogel proficiently mitigates the undue proliferation of EpiSCs in the presence of inflammation, thereby safeguarding the skin against hyperplasia and desquamation. Concurrently, it facilitates an augmentation in the functionality of the epidermal barrier. This holds potential therapeutic value for other inflammatory skin diseases such as psoriasis and atopic dermatitis, warranting further experimental exploration. Furthermore, the potential applications of Se-Met@GelMA hydrogel in diseases related to ferroptosis and aging in other organ systems urgently require further exploration, such as in inflammatory bowel disease or rheumatoid arthritis.

The condition of chronic wounds is highly dynamic and exhibits individual complexity influenced by various local and systemic factors [58]. Given the complexity of multi-stage functional decline during wound healing process in aging skin, employing tailored mesoporous inorganic biomaterials for the delivery of extracellular vesicle from engineered organoid or bacteria, could represent a promising therapeutic strategy [59–63]. The implantation of biomaterial scaffolds during the wound healing process could inevitably lead to host immune responses [64]. Employing single-cell sequencing and spatial transcriptomics to explore the characteristics of the immune microenvironment during skin aging, and developing immunomodulatory hydrogels to balance the immune response and wound healing progress, will contribute to perfecting skin regeneration [65].

To achieve optimal therapeutic efficiency for chronic wounds, there is a need for platforms capable of dynamically identifying individual anomalies and facilitating drug delivery with controlled release and minimal side effects. With the burgeoning growth of bioelectronics, the advancement of wearable electronics has transformed personalized daily disease management, surpassing traditional methods that may require prolonged hospitalization or patient intervention, significantly enhancing patient compliance [66–68]. Wearable sensors have been developed for precise measurement of wound biomarkers and provide round-the-clock wound monitoring [69]. Therefore, integrating the latest advancements in biomaterial science and digital health interventions with wearable wound bioelectronics offers a route to localized and controlled therapeutic delivery without disrupting the patient's daily activities [70]. This presents a future direction for the treatment and care of chronic wounds.

## 4. Conclusion

Based on the combined analysis of transcriptome sequencing and untargeted metabolomics, we identified age-dependent changes in *Gpx* gene family and metabolic networks of AA. AA was found to increase in aging skin, and can trigger lipid peroxidation and mitochondrial damage in GPX4 deficient EpiSCs, and induce cell ferroptosis. Se-Met can promote the expression of GPX4 with effective ultraviolet absorption and antioxidative capacities, helping EpiSCs resist mitochondrial damage and ferroptosis induced by AA. Se-Met@GelMA hydrogel has been shown to effectively accelerate wound healing in chronological aging model, and mitigate inflammation and lipid peroxidation in photoaging model. These characteristics render Se-Met@GelMA hydrogel valuable in practical clinical applications.

## 5. Materials and mehods

### 5.1. Ethics statement

All experimental procedures described herein were examined and approved by the Ethics Committee of our hospital. Animal experiments were carried out in accordance with the National Institutes of Health Guide for the Care and Use of Laboratory Animals, and were authorized by the Animal Care Committee. Young (3–6 month), middle (10–14 month) and old (18–24 month) male C57BL/6J mice, and BALB/c-nu female mice (2 month) were purchased from SPF (Beijing) Biotechnology Co., Ltd. All human specimens were obtained from the discarded thin split-thickness grafts during the skin grafting operation. All patients were advised about the experimental goals and volunteered to participate, with the written informed permission acquired.

### 5.2. Specimen acquisition

The tumor-free male C57BL/6J mice of the young and the old were further screened for good hair coats. Those with clear evidence of scratches, inflammation, or dermatitis were discarded. For the specimen acquisition, after the mice were anesthetized with isoflurane gas, depilation was performed and 8-mm biopsy punches were used to make two full-thickness (epidermis + dermis) wounds on both sides in the middle back of each mouse as described before [71]. 9 mice were randomly selected in each age group, with totally 18 skin samples collected for each group, half of which was used for omics analysis and protein detection, and the other half was used for pathological detection. As for omics analysis and protein detection, the collected skin samples were rinsed in PBS with the subcutaneous fat removed via a sterilized scalpel. Then, the samples were placed with the dermis side facing downward in 2.4 U/mL Dispase II (17105041, Gibco, USA) for 1 h to separate the dermis from the epidermis. The remaining epidermis, after undergoing enzymatic dissociation into single cells, was processed through flow cytometry to isolate EpiSCs. These isolated EpiSCs were then immediately frozen in liquid nitrogen for further experiments. As for pathological detection, the skin samples were immersed in 4% paraformaldehyde overnight, then for HE, Immunofluorescence, TUNEL staining, MASSON staining and EVG staining.

Clinical skin samples were obtained and kept in pre-chilled PBS and transported at 2–8 °C to the laboratory for processing. After rinsing with pre-chilled PBS, tissues were immersed in paraformaldehyde overnight, then for pathological staining. The remained tissues were preserved for

primary EpiSCs extraction and culture.

### 5.3. Transcriptomics analysis

For transcriptomics analysis, EpiSCs samples were homogenized in TRIzol reagent for total RNA extraction. RNA concentration and quality were gauged by NanoDrop 2000 (Thermo Fisher, USA). Approximately 5 μg of total RNA was employed for establishing the paired-end RNA-seq library for transcriptome sequencing on the Illumina HiSeq 2000 platform assisted by TIANGEN BIOTECH (BEIJING) Co., Ltd. With the low-quality reads trimmed and the adapters removed, clean RNA-Seq reads were mapped to the reference genome using Tophat2 (version 2.0.13). HTSeq was applied to calculate the number of unique mapped reads that mapped to an aviary gene model. Gene expression levels were measured as fragments per kilobase million (FPKM). Student's *t*-test was employed for statistical analysis. RNA-seq data were deposited in the Sequence Read Archive database (accession number: PRJNA957591). N = 9 for each group.

### 5.4. Sample preparation and LC-MS/MS analysis for metabolomics

EpiSCs samples were lysed in 80% aqueous methanol solution containing 0.1% formic acid. After vortex and ice bath, the samples were centrifuged at 15000 *g* for 10 min at 4 °C. Samples were diluted with mass spectrometry grade water to a final methanol content of 53% and then centrifuged at 15000 *g* for 10 min at 4 °C. The filtrate obtained after centrifugation was collected and analyzed via a Thermo Vanquish UHPLC system (Thermo Fisher, USA) directly connected to a Thermo QE system (Thermo Fisher, USA), assisted by TIANGEN BIOTECH (BEIJING) Co., Ltd. An equal volume of each sample was mixed and pooled as the Quality Control (QC) sample, to monitor instrument status and equilibrate the chromatographic-mass spec system before injection. The blank sample was 53% methanol containing 0.1% formic acid. The LC column employed was a Thermo Hypersil Gold column (C18) at 40 °C with a flow rate of 0.2 mL/min. Mobile phase A was 0.1% formic acid and mobile phase B was methanol in positive mode. For the negative mode, mobile phase A was 5 mM ammonium acetate (pH 9.0) and mobile phase B was methanol with the proportion gradually increased from 2% to 100% over 14 min. Each mass spectrum was scanned from *m/z* 70–1050. The settings of the ESI source were as follows: sheath gas flow rate: 35 arb, spray voltage: 3.2 kV, capillary temperature: 320 °C, and aux. gas flow rate: 10 arb. The ESI source settings were as follows: Polarity, Positive/Negative. MS/MS scans were data-dependent scans. N = 9 for each group. Multiple hypothesis testing was utilized for metabolomics data analysis.

### 5.5. Data analysis for metabolomics

The raw data generated by LC-MS/MS were processed with Compound Discoverer 3.1 (CD3.1, Thermo Fisher, USA) including peak alignment, peak selection and quantification for metabolites. The main parameters were set as follows: actual mass tolerance was 5 ppm; signal-to-noise ratio was 3; retention time tolerance was 0.2 min; signal intensity tolerance was 30%; and minimum intensity was 100000. Afterwards, peak intensities were normalized to the total intensity of the spectrometry. Normalized data were used to predict molecular formulas based on molecular ion peaks, additive ions and fragment ions. Peaks were then matched with mzCloud (https://www.mzcloud.org/), mzVault, and MassList databases for accurate and relative quantification. Statistical analysis was performed with R (version 3.4.3), Python (version 2.7.6) and CentOS (version 6.6). For non-normally distributed data, the area normalization method was applied. Then, the metabolites were annotated using the Human Metabolism Database (HMDB, Version 4.0) and Lipidmaps database. MetaX was employed for the OPLS-DA. To account for the differences in the amount of EpiSCs, the intensities were normalized using quantile normalization. Statistical significance was compared via the Student's *t*-test.

### 5.6. Mouse treatment

In the previous experiments of the lab, we have confirmed the reduced expression of GPX4 in the epidermis of middle-aged mice compared with young mice. Thus, middle-aged mice were selected to investigate whether AA could induce ferroptosis in GPX4-deficient EpiSCs in vivo. The young and middle-aged healthy male C57BL/6J mice were randomly assigned to the control group or the experimental group, and received daily PBS or AA (10 mg) via oral gavage over the course of one month. During the experiment, mice were fed chow diet ad libitum, and then were sacrificed for tissue collection. N = 6 for each group.

### 5.7. Preparation of the acrylate pegylated Se-Met (AC-PEG-Se-Met)

2 kDa AC-PEG-NHS (EFL, China) was dissolved at room temperature with Se-Met (10 μM) at a molar ratio of 1:10 (AC-PEG-NHS: Se-Met) in PBS at pH 8.0. After 5 min of vibration, the solution was incubated 4 °C for 18 h. The unconjugated Se-Met was removed by dialysis for 72 h. After freeze-drying, the product underwent X-ray Photoelectron Spectroscopy (XPS), $^{1}$H Nuclear Magnetic Resonance, and UV–Vis spectroscopy for a comprehensive structural evaluation. AC-PEG-Se-Met was suspended in PBS (pH 7.4), aliquoted and stored at −80 °C for further use.

### 5.8. GelMA hydrogel synthesis

The lithium acylphosphinate (LAP) photoinitiator, and GelMA were synthesized under the assistance of the Engineering for Life Co., Ltd. LAP was dissolved in PBS for a final concentration of 0.5% (w/v), heated at 55 °C for 15 min and then after it cooled, an equal volume of PBS containing 10 μM AC-PEG-Se-Met was added to the solution to achieve a final concentration of 0.25% LAP and 5 μM AC-PEG-Se-Met. Then, corresponding mass of GelMA was added to the solution to fabricate hydrogels respectively in the concentration (w/v) of 5%, 10% and 15%. The hydrogel solution was passed through a 0.22 μm filter for sterility. After chemically cross-linked by 10 mW/cm$^2$ UV light (365 nm) for 15 s, the hydrogels were immersed in PBS in a 12-well plate and the supernatant was collected for 15 consecutive days. The AC-PEG-Se-Met content in the supernatant was detected using ICP-MS.

### 5.9. Full-thickness skin defect model

The aged healthy male C57BL/6J mice were randomly assigned into 4 groups: Ctrl (treated with PBS), GelMA (treated with GelMA), Se-Met (treated with AC-PEG-Se-Met), and Se-Met@GelMA (treated with Se-Met@GelMA). The model was established following the aforementioned method [72]. Briefly, the mice were anesthetized with Isoflurane and full-thickness skin defects with a diameter of 8 mm were created on their backs. The wounds were processed to prevent contracture immediately after modeling, and 10-mm-diameter blue fenestrated sheets were used as a reference to measure the residual wounds at indicated time points. After model establishment, mice in the Ctrl and Se-Met groups were given a daily dosage of 100 μL PBS or AC-PEG-Se-Met (5 μM) which were dropped onto the wound surface. The GelMA and Se-Met@GelMA groups received 100 μL of 10% corresponding hydrogels immediately after injury and again on the seventh day, and were cross-linked using 365 nm light for 15 s on the wound surface. On the 4th, 7th, 10th and 14th days after modeling, the wound area was quantitatively analyzed using ImageJ software after taking pictures of 4 randomly selected mice with 8 wounds. The wound healing rate was calculated as (1 – residual wound area/total wound area) × 100%. All measurements were performed in a blinded way.

### 5.10. Photoaging model

BALB/c-nu female mice were randomly assigned into five groups, each comprising six mice. The Ctrl group was not exposed to UVB irradiation. For the UV-exposed mice, the UVB irradiation intensity was set at 1000 μW/cm$^2$, delivering a total energy exposure of 1.5 J/cm$^2$ over a period of 300 s for five consecutive days. GelMA hydrogels, infused with varying concentrations of AC-PEG-Se-Met (0, 2.5, 5, 10 μM), were uniformly applied to the dorsal skin of the mice for 30 min prior to each UVB exposure session. Daily photographic documentation of the dorsal skin was conducted, and the skin lesions was assessed by two dermatologists, providing an expert evaluation of the photodamage.

### 5.11. Statistical analysis

The analysis was performed in a blinded way. Excel and SPSS were utilized to process the data. Continuous variables were first tested for normality by the Kolmogorov-Smirnov test, then for Homogeneity of variance test. Normally distributed data were presented as mean ± standard deviation and tested using two-tailed unpaired Student's *t*-test or one-way ANOVA test followed by the multiple comparisons Bonferroni test. 0.05 is referred to as the level of significance.

## Consent for publication

This manuscript has not been published and is not under consideration for publication elsewhere. The details of the manuscript can be published and all the authors providing consent have been shown the article contents to be published.

## Financial disclosure statement

All authors have nothing to disclose.

## Data access statement

Further information and requests for reagents may be directed to and will be fulfilled by the Lead Contact: Prof. Chuanan Shen (shenchuanan@301hospital.com.cn).

## Ethics approval

All animal experimental protocols were approved by the Animal Research Ethics Committee of the Fourth Medical Center of Chinese PLA General Hospital (approval number: 82072169, 82272279), and complied with the rules of the specific pathogen-free animal laboratory. All methods followed the guidelines for animal subject care and use outlined in the Guide for the Care and Use of Laboratory Animals (Institute of Laboratory Animal Resources, National Academy of Sciences, Bethesda, MD, USA). Written informed consent to participate in the study was provided by all the patients.

## CRediT authorship contribution statement

**Jiachen Sun:** Writing – original draft, Methodology, Investigation. **Xiaoye Xie:** Writing – review & editing, Methodology. **Yaoyao Song:** Writing – review & editing, Visualization, Validation. **Tianjun Sun:** Writing – review & editing. **Xinzhu Liu:** Writing – review & editing. **Huageng Yuan:** Writing – review & editing. **Chuanan Shen:** Writing – review & editing, Supervision, Resources, Project administration, Methodology, Investigation, Funding acquisition, Conceptualization.

## Declaration of competing interest

The authors declare that the research was conducted in the absence of any commercial or financial relationships that could be construed as a potential conflict of interest.

## Acknowledgements

This study was supported from the Program of National Natural Science Foundation of China (82272279, 82072169).

## Appendix A. Supplementary data

Supplementary data to this article can be found online at https://doi.org/10.1016/j.bioactmat.2024.02.013.

## References

[1] L. N, et al., Stem cell competition orchestrates skin homeostasis and ageing, Nature 568 (7752) (2019) 344–350.
[2] S. Horvath, K. Raj, DNA methylation-based biomarkers and the epigenetic clock theory of ageing, Nat. Rev. Genet. 19 (6) (2018) 371–384.
[3] Y. Lu, et al., Reprogramming to recover youthful epigenetic information and restore vision, Nature 588 (7836) (2020) 124–129.
[4] A.J. Covarrubias, et al., NAD(+) metabolism and its roles in cellular processes during ageing, Nat. Rev. Mol. Cell Biol. 22 (2) (2021) 119–141.
[5] A. Bratic, N.G. Larsson, The role of mitochondria in aging, J. Clin. Invest. 123 (3) (2013) 951–957.
[6] Z. Mei, et al., Association between the Metabolome and Bone Mineral Density in a Chinese Population, EBioMedicine, 2020, p. 62.
[7] H. Clevers, K.M. Loh, R. Nusse, Stem cell signaling. An integral program for tissue renewal and regeneration: Wnt signaling and stem cell control, Science 346 (6205) (2014) 1248012.
[8] C. Wei, M. Wang, X.-J. Wang, Evolutionary conservation analysis of human arachidonic acid metabolism pathway genes, Life Medicine 2 (2) (2023) lnad004.
[9] M. Cioce, et al., Arachidonic acid drives adaptive responses to chemotherapy-induced stress in malignant mesothelioma, J. Exp. Clin. Cancer Res. 40 (1) (2021) 344.
[10] S.Y. Oh, et al., Arachidonic acid promotes skin wound healing through induction of human MSC migration by MT3-MMP-mediated fibronectin degradation, Cell Death Dis. 6 (5) (2015) e1750.
[11] H. Meves, Arachidonic acid and ion channels: an update, Br. J. Pharmacol. 155 (1) (2008) 4–16.
[12] T.S. Hallstrand, et al., Regulation and function of epithelial secreted phospholipase A2 group X in asthma, Am. J. Respir. Crit. Care Med. 188 (1) (2013) 42–50.
[13] S. Shao, et al., Phospholipase A2 enzymes represent a shared pathogenic pathway in psoriasis and pityriasis rubra pilaris, JCI Insight 6 (20) (2021).
[14] J. Lou, et al., Inhibition of PLA2G4E/cPLA2 promotes survival of random skin flaps by alleviating Lysosomal membrane permeabilization-Induced necroptosis, Autophagy 18 (8) (2022) 1841–1863.
[15] N.K. Biswas, et al., Somatic mutations in arachidonic acid metabolism pathway genes enhance oral cancer post-treatment disease-free survival, Nat. Commun. 5 (2014) 5835.
[16] R. Brigelius-Flohé, L. Flohé, Regulatory phenomena in the glutathione peroxidase superfamily, Antioxidants Redox Signal. 33 (7) (2020) 498–516.
[17] J.A. Fafián-Labora, J.A. Rodríguez-Navarro, A. O'Loghlen, Small extracellular vesicles have GST activity and ameliorate senescence-related tissue damage, Cell Metabol. 32 (1) (2020) 71–86.e5.
[18] S. Xu, et al., Age-associated changes in GSH S-transferase gene/proteins in livers of rats, Redox Rep. 23 (1) (2018) 213–218.
[19] A. Kuehne, et al., An integrative metabolomics and transcriptomics study to identify metabolic alterations in aged skin of humans in vivo, BMC Genom. 18 (1) (2017) 169.
[20] K. Papsdorf, A. Brunet, Linking lipid metabolism to chromatin regulation in aging, Trends Cell Biol. 29 (2) (2019) 97–116.
[21] A. Anderson, et al., 7-Ketocholesterol in disease and aging, Redox Biol. 29 (2020) 101380.
[22] T. Nury, et al., Attenuation of 7-ketocholesterol- and 7β-hydroxycholesterol-induced oxiapoptophagy by nutrients, synthetic molecules and oils: potential for the prevention of age-related diseases, Ageing Res. Rev. 68 (2021) 101324.
[23] M.S. Mortensen, J. Ruiz, J.L. Watts, Polyunsaturated fatty acids drive lipid peroxidation during ferroptosis, Cells 12 (5) (2023).
[24] G. Aldini, et al., Intervention strategies to inhibit protein carbonylation by lipoxidation-derived reactive carbonyls, Med. Res. Rev. 27 (6) (2007) 817–868.
[25] L. Mayr, et al., Dietary lipids fuel GPX4-restricted enteritis resembling Crohn's disease, Nat. Commun. 11 (1) (2020) 1775.
[26] S. Terlecki-Zaniewicz, et al., Biomolecular condensation of NUP98 fusion proteins drives leukemogenic gene expression, Nat. Struct. Mol. Biol. 28 (2) (2021) 190–201.
[27] A. Razaghi, et al., Selenium stimulates the antitumour immunity: insights to future research, Eur. J. Cancer 155 (2021) 256–267.
[28] E. Domínguez-Álvarez, et al., Selenium and tellurium in the development of novel small molecules and nanoparticles as cancer multidrug resistance reversal agents, Drug Resist. Updates 63 (2022) 100844.
[29] Y. Yao, et al., Selenium-GPX4 axis protects follicular helper T cells from ferroptosis, Nat. Immunol. 22 (9) (2021) 1127–1139.

[30] Y. Liang, J. He, B. Guo, Functional hydrogels as wound dressing to enhance wound healing, ACS Nano 15 (8) (2021) 12687–12722.
[31] Y. Fan, et al., One ternary nucleic acid delivery system with smart dextran-peptide coating enables in vivo and ex vivo wound therapy, Matter 6 (1) (2023) 239–259.
[32] R. Dimatteo, N.J. Darling, T. Segura, In situ forming injectable hydrogels for drug delivery and wound repair, Adv. Drug Deliv. Rev. 127 (2018) 167–184.
[33] C. Cai, et al., Self-healing hydrogel embodied with macrophage-regulation and responsive-gene-silencing properties for synergistic prevention of peritendinous adhesion, Adv. Mater. 34 (5) (2022) e2106564.
[34] S. Li, et al., Gelatin methacryloyl (GelMA) loaded with concentrated hypoxic pretreated adipose-derived mesenchymal stem cells(ADSCs) conditioned medium promotes wound healing and vascular regeneration in aged skin, Biomater. Res. 27 (1) (2023) 11.
[35] Y. Lin, et al., Single-cell RNA-seq of UVB-radiated skin reveals landscape of photoaging-related inflammation and protection by vitamin D, Gene 831 (2022) 146563.
[36] A. De Magis, et al., UV-induced G4 DNA structures recruit ZRF1 which prevents UV-induced senescence, Nat. Commun. 14 (1) (2023) 6705.
[37] A. Worrede, S.M. Douglass, A.T. Weeraratna, The dark side of daylight: photoaging and the tumor microenvironment in melanoma progression, J. Clin. Invest. 131 (6) (2021).
[38] S. Hu, et al., Needle-free injection of exosomes derived from human dermal fibroblast spheroids ameliorates skin photoaging, ACS Nano 13 (10) (2019) 11273–11282.
[39] X. Xue, et al., Recent advances in design of functional biocompatible hydrogels for bone tissue engineering, Adv. Funct. Mater. 31 (19) (2021) 2009432.
[40] C. Cui, et al., A janus hydrogel wet adhesive for internal tissue repair and anti-postoperative adhesion, Adv. Funct. Mater. 30 (49) (2020) 2005689.
[41] X. Ren, et al., Reactive oxygen species (ROS)-responsive biomaterials for the treatment of bone-related diseases, Front. Bioeng. Biotechnol. 9 (2022) 820468.
[42] Y. Wu, et al., An injectable supramolecular polymer nanocomposite hydrogel for prevention of breast cancer recurrence with theranostic and mammoplastic functions, Adv. Funct. Mater. 28 (21) (2018) 1801000.
[43] Q. Zhang, et al., A factor-free hydrogel with ROS scavenging and responsive degradation for enhanced diabetic bone healing, Small (2024) e2306389 **n/a**(n/a.
[44] C.D. Wiley, J. Campisi, The metabolic roots of senescence: mechanisms and opportunities for intervention, Nat. Metab. 3 (10) (2021) 1290–1301.
[45] D. Lv, et al., Targeting phenylpyruvate restrains excessive NLRP3 inflammasome activation and pathological inflammation in diabetic wound healing, Cell Reports Medicine 4 (8) (2023).
[46] G. Fan, et al., DHA/AA alleviates LPS-induced Kupffer cells pyroptosis via GPR120 interaction with NLRP3 to inhibit inflammasome complexes assembly, Cell Death Dis. 12 (1) (2021) 73.
[47] Y.L. Chen, et al., Adiponectin receptor PAQR-2 signaling senses low temperature to promote C. elegans longevity by regulating autophagy, Nat. Commun. 10 (1) (2019) 2602.
[48] G. Li, et al., WFDC12-overexpressing contributes to the development of atopic dermatitis via accelerating ALOX12/15 metabolism and PAF accumulation, Cell Death Dis. 14 (3) (2023) 185.
[49] L. Bai, P. Song, J. Su, Bioactive elements manipulate bone regeneration, Biomaterials Translational 4 (4) (2023) 248.
[50] L. Flohé, S. Toppo, L. Orian, The glutathione peroxidase family: discoveries and mechanism, Free Radic. Biol. Med. 187 (2022) 113–122.
[51] Y. Xie, et al., GPX4 in cell death, autophagy, and disease, Autophagy 19 (10) (2023) 2621–2638.
[52] I. Ingold, et al., Selenium utilization by GPX4 is required to prevent hydroperoxide-induced ferroptosis, Cell 172 (3) (2018) 409–422.e21.
[53] M. Vinceti, et al., Safety of selenium exposure and limitations of selenoprotein maximization: molecular and epidemiologic perspectives, Environ. Res. 211 (2022) 113092.
[54] B. Dong, et al., Selenomethionine alleviates decabromodiphenyl ether-induced oxidative stress and ferroptosis via the NRF2/GPX4 pathway in the chicken brain, J. Hazard Mater. 465 (2024) 133307.
[55] S. Fan, et al., Selenomethionine protects the liver from dietary deoxynivalenol exposure via Nrf2/PPARγ-GPX4-ferroptosis pathway in mice, Toxicology 501 (2024) 153689.
[56] X. Xue, et al., Rational design of multifunctional CuS nanoparticle-PEG composite soft hydrogel-coated 3D hard polycaprolactone scaffolds for efficient bone regeneration, Adv. Funct. Mater. 32 (33) (2022) 2202470.
[57] Y. Hu, Y. Li, F.-J. Xu, Versatile functionalization of polysaccharides via polymer grafts: from design to biomedical applications, Accounts Chem. Res. 50 (2) (2017) 281–292.
[58] Z. Shao, et al., Wound microenvironment self-adaptive hydrogel with efficient angiogenesis for promoting diabetic wound healing, Bioact. Mater. 20 (2023) 561–573.
[59] H. Liu, J. Su, Organoid extracellular vesicle-based therapeutic strategies for bone therapy, Biomaterials Translational 4 (4) (2023) 199.
[60] Y. Zou, et al., Tailored mesoporous inorganic biomaterials: assembly, functionalization, and drug delivery engineering, Adv. Mater. 33 (2) (2021) 2005215.
[61] H. Liu, J. Su, Organoid and organoid extracellular vesicles for osteoporotic fractures therapy: current status and future perspectives, Interdisciplinary Medicine 1 (3) (2023) e20230011.
[62] H. Song, et al., Reversal of osteoporotic activity by endothelial cell-secreted bone targeting and biocompatible exosomes, Nano Lett. 19 (5) (2019) 3040–3048.
[63] J. Pan, et al., Bacteria-Derived outer-membrane vesicles hitchhike neutrophils to enhance ischemic stroke therapy, Adv. Mater. 35 (38) (2023) 2301779.
[64] Y. Wang, et al., Bone repair biomaterials: a perspective from immunomodulation, Adv. Funct. Mater. 32 (51) (2022) 2208639.
[65] P. Wu, Y. Liang, G. Sun, Engineering immune-responsive biomaterials for skin regeneration, Biomater Transl 2 (1) (2021) 61–71.
[66] C. Wang, E. Shirzaei Sani, W. Gao, Wearable bioelectronics for chronic wound management, Adv. Funct. Mater. 32 (17) (2022) 2111022.
[67] S. Wu, et al., Biodegradable shape-memory ionogels as green and adaptive wearable electronics toward physical rehabilitation, Adv. Funct. Mater. 33 (36) (2023) 2303292.
[68] Y. Wang, et al., An autofluorescent hydrogel with water-dependent emission for dehydration-visualizable smart wearable electronics, Adv. Funct. Mater. 33 (19) (2023) 2213545.
[69] Y. Yang, W. Gao, Wearable and flexible electronics for continuous molecular monitoring, Chem. Soc. Rev. 48 (6) (2019) 1465–1491.
[70] C. Shang, et al., One 3D aerogel wearable pressure sensor with ultrahigh sensitivity, wide working range, low detection limit for voice recognition and physiological signal monitoring, Sci. China Mater. 66 (5) (2023) 1911–1922.
[71] J. Sun, et al., Adiponectin receptor agonist AdipoRon blocks skin inflamm-ageing by regulating mitochondrial dynamics, Cell Prolif. 54 (12) (2021) e13155.
[72] J. Sun, et al., Tideglusib promotes wound healing in aged skin by activating PI3K/Akt pathway, Stem Cell Res. Ther. 13 (1) (2022) 269.